GEM TN-93-349

The Scintillating Barrel Calorimeter: Optimization of Performance

Yu. Efremenko, Yu. Kamyshkov, A. Savin, K. Shomakov, E. Tarkovsky
ITEP(MOSCOW)/Oak Ridge National Laboratory

F. Plasil, M. Rennich, C. Wynn
Oak Ridge National Laboratory

April 5, 1993

Abstract;

This technical note describes the results of Monte Carlo simulations towards the design and optimal performance of the GEM Scintillating Barrel Calorimeter.

The Scintillating Barrel Calorimeter: Optimization of Performance

Yu. Efremenko[1] Yu. Kamyshkov[1] F. Plasil
M. Rennich A. Savin[1] K. Shmakov[1]
E. Tarkovsky[1]
C. Wynn

Oak Ridge National Laboratory *
([1]) ITEP(Moscow) / Oak Ridge National Laboratory

April 5, 1993
Revised June 20, 1993

Abstract

This Technical Note describes the results of Monte Carlo simulations towards the design and optimal performance of the GEM Scintillating Barrel Calorimeter.

---

*Managed by Martin Marietta Energy Systems, Inc., under contract DE-AC05-840R21400 with the U.S. Department of Energy

Introduction

The choice of calorimeter technology made by GEM includes, in the barrel region, liquid krypton EM and hadronic calorimeters with a total radial thickness of 6λ, followed by a cylindrical scintillating barrel calorimeter layer (Figure 1) with an absorbtion thickness of 4.5λ. Both the EM and hadronic sections of the two endcaps employ the liquid Ar technique with a total instrumented thickness of $\approx 8\lambda$. Passive copper absorber is used in the end caps behind the noble liquid cryostats to provide additional absorbtion length. Both EM and hadronic sections of the noble liquid calorimeter are longitudinally segmented (3 segments in the EM section and 3 segments in the hadronic section of the liquid barrel calorimeter).

The role and the goals of the Scintillating Barrel Calorimeter (SBC) are defined as follows:

a) In a mechanical sense, it serves primarily as a structural support for the three noble liquid calorimeter cryogenic vessels and for the passive absorbers of the endcaps with embedded forward hadron calorimeters; it also helps to accommodate cryogenic and other connection services.

b) Since the major part of the jet energy is measured in the noble liquid section, the SBC should serve as a "tail catcher" for these measurements, allowing no degradation of the constant term in the jet energy resolution, i.e., SBC should be instrumented. The level of instrumentation, however, should be minimal so as to keep the total cost of the GEM calorimeter at a minimum.

c) With the SBC device being instrumented at the level necessary for hadronic jet measurements, one should also be able to obtain information pertinent to the muon system: energy deposition in the SBC and position information through the transverse segmentation of the SBC.

We have undertaken Monte Carlo simulations to address the above issues and to study the performance of the GEM calorimeter system as it relates to the SBC instrumentation configuration. The major question addressed by these simulations was: what is a sufficient minimum level of instrumentation for the SBC device? We have not addressed the issue of optimal depth division between the noble-liquid and scintillating-calorimetry sections in the barrel, even though we are aware that the present division might not be optimum both in terms of performance and in terms of the overall cost.

Chapter 1 of this technical note describes the mechanical design of the scintillating barrel calorimeter as it was used in the Monte Carlo calculations. This design also reflects the feedback of the Monte Carlo simulations with respect to the number of active instrumented scintillating layers in the SBC. In chapter 2 hadronic jet resolution for the whole GEM barrel calorimeter (LKr and SBC) is discussed for different number of instrumented layers (from 0 to 10) in the SBC. Chapter 3 addresses the importance of instrumentation in the SBC for measurements of missing E_T in the GEM detector. In chapter 4 the detection of muons and corrections for muon energy losses in the GEM barrel calorimeter are considered. Finally, chapter 5 is devoted to simulations of light transport in the scintillating tiles with WLS fiber readout.

1 Scintillating Barrel Calorimeter

The scintillating barrel calorimeter is composed of 44 absorber/scintillating tile modules mounted inside a 70-mm-thick stainless steel support tube. Each module covers half the length of the barrel (Figure 1); thus, each end of the barrel has 22 radial modules (Figure 2). The support tube is attached inside the GEM detector to the Central Detector Support (CDS) (Figure 3). A 100-mm-thick layer of copper on the outside of the support tube is grooved to provide clearance for utility lines required for the central tracker and for the liquid calorimeter (Figure 4).

The modules of the Scintillating Barrel Calorimeter are about 57-cm thick, 100-cm wide, and 500-cm long, with weight of about 24 Mg each. The modules have layers of absorber plates interleaved with four layers of readout tiles (Figure 4). The plates are bolted together (with 5-cm-diameter rods), and spacers are used to create gaps for scintillating plates. The scintillating modules are completely self-contained and self-supporting. They are bolted to the outer structural support tube which also serves as the primary liquid calorimeter support.

Copper (or brass) was chosen as the absorber material to provide maximum absorption length at minimal cost. Modular construction has been used to simplify the manufacturing, transportation and assembly (Figure 5).

Connection of the support tube to the CDS will be accomplished via stand-off frames which are designed to accommodate the large cabling and piping bundles which will be routed through the CDS. The stand-off frames will be welded to the support tube and bolted to the CDS in order to reduce the complexity of the assembly operations. A finite element analysis of the scintillating hadron barrel indicates that the constraining criterion is the amount of deflection resulting from the support of the liquid system and passive end caps. The predicted full load deflection of the system is approximately 1.0 cm.

The 640 PMT readout/calibration assemblies will be mounted in clusters located between the liquid system electronics junction boxes. Each readout assembly is expected to produce approximately 1 to 2 watts of power. Heat resulting from the assemblies will be removed via the same forced water heat-exchanger system required for the noble liquid electronics.

All the utilities and readout cabling for the tracker, noble liquid calorimeter, forward calorimeter and scintillating barrel will be routed around the outside of the barrel. The piping and cables will be embedded in grooves in a 100-mm layer of brass.

There are four layers of scintillating tiles in the scintillating barrel. The first layer samples the hadronic jets/showers after the dead material of the outer cryostat walls and after the first absorber layer of the scintillating modules. The other three layers are equally spaced in the absorber, 13 cm apart.

The scintillating layers are made of 6-mm-thick tiles forming projective towers of size $\Delta\Theta$ x $\Delta\varphi$ = 0.16 x 0.16 (matching 2 x 2 hadronic towers in the liquid hadron calorimeter). The size of the tiles in the tower is approximately 8 cm x 48 cm at 90°and 8 cm x 87 cm at the end of the barrel. Each tile is read out by one or two wave length shifting (WLS) fibers embedded in the scintillator as shown in Figure 6. The WLS fibers (1- or 2-mm diameter) are parallel to the z-axis and optically glued in a U-shaped groove. (Non-glued WLS fiber is being considered as an option for R&D studies.) The far end of the WLS fiber is mirrored to increase the collection of light. The WLS fibers are slightly (10-20 cm) longer than the length of the tile and positioned in the grooves such that the exiting end protrudes above the neighboring tile (Figures 4 and 6). The WLS fiber ends are spliced to the clear transport fiber with the aid of a thin plastic sleeve. The scintillating tiles are wrapped in aluminized mylar or in some other reflecting material. All fiber connections and transport fibers are laid and fixed in the 12-mm gap between absorber plates during the module assembly. The gaps between the absorber plates are maintained by spacers. Eight tiles in Θ by 12 rows in φ constitute one scintillator layer in the module. Fibers from four layers within one 0.16 x 0.16 tower, or a total of 24 tiles, are read out by one photomultiplier tube (see Figure 7). The total number of channels in the system is 640. Since the modules are only half-barrel long, the readout assemblies of the modules are located on one end of each module or on both ends of the barrel.

Major characteristics and parameters of the Scintillating Barrel Calorimeter (SBC) are given in the Table 1. The passive assembly is shown in Figure 8. It will be constructed as a single module at the SSCL by bolting copper or brass plates to form a ring. A structural tube will be located inside the plates to support the forward calorimeter.

For large PMT-based systems, several tested calibration methods and monitoring techniques are available to attain several percent tower-to-tower and module-to-module calibration with good overall stability. In general, these techniques involve use of radioactive sources and flashing light sources. The energy flow measurement is another candidate for calibration and monitoring. One can transfer the absolute calibrations of a few beam-tested cells onto the entire detector by measuring the average energy deposited from all pp-interactions once the eta variation is known.

2 Optimization of the number of sensitive layers by simulation of jet resolution

Monojets were generated by the LUND single-jet generator. The total energy of the jets was rescaled to the initial fixed value. Particles were transported by GEANT 3.15 (GHEISHA) with 10 KeV cuts for electrons, gammas, hadrons, and neutrons. Jets were generated with the energies of 10 GeV, 25 GeV, 100 GeV, 250 GeV and 1 TeV and with statistics of 2272, 2152, 724, 621 and 830 events, correspondingly.

The geometry of the calorimeter described in Chapter 1 was used with the following simplifications:

1. The accordion EM calorimeter was replaced for the purposes of this simulation, with an equivalent parallel plate scheme with 1.4-mm Pb/5.7-mm LKr layers, and with 3 depth segments of $4X0 + 8X0 + 13X0 +$

dead material both in front and behind the EM section.

2. The liquid HC section was defined as 2.0-mm LKr/9.0-mm Pb plates with 3 depth segments of $1.25\lambda + 1.25\lambda + 2.5\lambda$ + dead material behind the HC section and between the segments.

3. The SBC section consisted of 10 layers, each consisting of 3.5-mm scintillator followed by 57-mm copper. Dead regions between SBC modules, spacers, tightening rods, and structural membranes were not simulated.

Events generated with the 10-scintillator-layer SBC configuration were also used to study setups with fewer layers. It was possible, for example, for a 4-layer configuration to choose an optimum combination of 4 out of the 10 layers by layer permutations. Depth segmentation of the liquid EM and HC sections allowed the assignment of individual weights to each segment during the event analysis. These weights were obtained as a result of minimization of the overall width of the jet response spectra at each jet energy.

Our previous simulations of the performance of copper/scintillating fiber (spaghetti) calorimeter and comparison of these simulations with the measurements done at BNL in the summer of 1992 (see Fig. 9) give us some confidence that GEANT can adequately describe copper/scintillator calorimeter structures at least in the measured hadron energy range of 5-20 GeV. GEANT/GHEISHA parameters used for spaghetti simulations, together with the appropriate value of Birks coefficient for plastic scintillator, were used to simulate the response of the GEM SBC.

Unfortunately, no data are available for LKr/Pb hadron calorimeter structures to make similar GEANT/GHEISHA comparisons. Consequently, the absolute values of the global energy resolution predicted by our simulations may require a systematic correction. Nevertheless, we believe that the relative effects of SBC instrumentation on the global resolution are correctly reproduced. CALOR89 simulations for pions in the GEM liquid Kr/Pb calorimeter recently performed by B.Moore [5] give a hadronic resolution similar to that of our GEANT/GHEISHA simulations.

The SBC makes it possible to correct for the back leakages from the liquid barrel (Fig. 10) and endcap calorimeters in front of it. This correction is important for jet energies larger than 50 GeV. Most events produce essentially no signals, but some events have long tails which extend up to 70% of the total jet energy (see Fig. 11-Fig. 15).

Weights were determined from the following two constraints:

1. Minimum of RMS — this provides a system of linear equations.
2. Linearity — mean energy at each energy point must be equal to generated jet energy.

The procedure for obtaining the weights consists of the following steps :

1. Weights are first calculated with full statistics.
2. For events contained within $\pm 2\sigma$ around the mean value, the weights are recalculated. This makes the result insensitive to rare events involving large fluctuations, even though the weights do not change significantly from step 1 to step 2.
3. Weights calculated with 50% of events were compared to those obtained from the other 50% to check the stability of the procedure. No difference was observed between the two results.

Calculated weights are shown in Fig. 16 – Fig. 18. Smooth (vs E^{jet}) behaviour of weights for EM and hadronic parts of liquid calorimeter should be a guarantee for stable energy reconstruction procedure at all energies. For low-energy jets, the SBC weights are not important since the corresponding contribution is small.

Seven depth segments (3 in EM, 3 in HC, one in SB) give the possibility of effective corrections for losses in dead material. To some extent, energy leakages can also be corrected by measurements of the energy deposited in the last section of the liquid hardon calorimeter (see section III in Fig. 17), but small fraction of the events (less than 1%) with large leakages can be corrected only by SBC measurements. This can be seen from the comparison of non-segmented liquid EM and HC response (Fig. 19) with the response obtained with 3 segments in the EM and 3 segments in the HC sections (Fig. 20).

For high energy jets (see Fig. 20) SBC measurement improves both resolution and the leakage effects in the calorimeter response. Jet resolution was parametrized by $\sqrt{\frac{A^2}{E} + B^2}$, where A is the stochastic term, B the constant term, and E the jet energy in GeV (Fig. 21). The effect of SBC instrumentation is an improvement in the constant term of jet energy resolution

from 5.6 to 4.8% in the case of non-segmented EM and HC and
from 4.8 to 3.7% in the case of 3 segments in EM, 3 segments in HC.

Figure 22 shows single-pion energy resolution for the same calorimeter configurations. Weights for the pion response were calculated with a procedure similar to that described above.

Jet resolution was optimized as a function of the number and position of scintillating layers in the SBC. Results are shown in Table 2 and in Fig. 23. Optimum position of layers naturally corresponds to a uniform sampling distribution within the SBC absorber.

Conclusion

1. An instrumented SBC improves the constant term in jet energy resolution from 4.8% to 3.7%.
2. Longitudinal segmentation of the liquid EM and HC is as important for good jet energy resolution as the whole instrumented SBC, though rare large leakages can only be corrected by means of the SBC.
3. Increasing the number of instrumented layers in the SBC beyond 4 does not result in an improvement in the constant term of the resolution function.

3 Missing E_T

Missing E_T physics is one of the important elements of the GEM physics program [1]. Many new objects – supersymmetric particles (gluino, neutralino etc.), t-quark and new exotic particles – can potentially be found by means of missing E_T measurements. To achieve the required discovery potential for the new physics, the GEM detector has to be capable of measuring missing E_T energy correctly above 100 GeV [1].

Jets in the barrel region which have high p_T can deposit some part of their energy in the SBC. If the SBC is not instrumented, or not sufficiently instrumented, this might result in a spurious missing E_T signal. The longitudinal segmentation in the liquid calorimeter sections might help to estimate the amount of energy leaked out into the SBC section. However, if the

SBC section is not instrumented, some fluctuations, as, for example, the one shown on Fig. 24, cannot be compensated for by measurements in the liquid calorimeter.

Results of instrumentation of the SBC on missing E_T are also discussed in a GEM note [2]. Realistic reproductions of jet hadronic shower fluctuations in the SBC in MC simulations are needed since these fluctuations are the source of the missing E_T. Using GEANT for simulation of jets is very time consuming. We choose instead a scheme in which the probability of the energy fluctuations in the SBC is parametrized for different hadron energies and at different depths (see ref. [2] for more details). To estimate the contribution of the fluctuations, the following steps were taken.

1. A full GEANT simulation of individual hadrons was undertaken. π^- of different energies were generated using GEANT 3.15 in the GEM geometry with cuts 50 keV for photons, 100 keV for electrons and 1 MeV for hadrons. Examples of distributions of the energy deposition in the SBC for π^- of different energies are presented in Fig. 25. The result of parametrization of the probability for the hadron energy loss in the SBC is shown in Figs. 26 and 27 for two energy-loss ranges. These distributions (note the logarithmic vertical scale) were used for the simulation of the energy losses in the SBC.

2. Jets produced by PYTHIA 5.6 event generator in different p_T bins were used with the above parametrization to pick up randomly the energy deposition in the SBC for all of the hadrons in a jet. This energy deposition, in case of no measurements in the SBC, will contribute directly to the missing E_T signal. Jets produced in different p_T bins have different cross-sections. The results of fluctuations of energy deposition in the SBC were added, with weights proportional to these cross-sections. The missing E_T was calculated for an idealized GEM detector, which had full η coverage, perfect energy and position resolution, and no cracks or dead regions. Only neutrinos were allowed to leak out of the calorimeter as well as fluctuating tails of hadronic jets due to non-instrumented SBC. The missing E_T spectrum resulting from a non-instrumented SBC is compared to the Standard Model missing E_T background spectrum produced by cascade quark decays in Fig. 28. Each of the contributions was calculated separately. In the same picture, the spectrum of individual hadrons from the jets is

shown. This spectrum has a 3-orders-of-magnitude higher cross section than the missing E_T spectrum resulting from SBC measurements.

3. Finally, the missing E_T effects, which are a consequence of a non-instrumented SBC, were combined with the missing E_T effects produced in the forward calorimeter via leakages beyond $\eta = 5.0$. In Fig. 29 this combined missing E_T spectrum is compared with the neutrino background predicted on the basis of the Standard Model.

From the figures mentioned above, one can conclude that the missing E_T spectrum induced by a non-instrumented SBC is about one order of magnitude below that expected from the Standard Model neutrino. Both have tails which extend to the TeV region. Using the signals from an instrumented SBC and the longitudinal segmentation of the EM and Hadron Calorimeters, one suppresses this spurious missing E_T background. To calculate correctly the missing E_T spectrum with an instrumented SBC, one should use a simulation technique different from that used by us. One can see (Fig. 29) that the effect of limited forward calorimeter coverage dominates over the neutrino background for $E_T < 100$ GeV. (This conclusion was reached in Ref. [3].)

A correlation also exists between the direction of the missing E_T vector and the direction of energetic muons in the same event, as shown in Fig. 30 for the Standard Model neutrino events. Similarly a correlation of the missing E_T vector with the detected portion of jets exists for most of the background events resulting from instrumental or calorimeter non-perfection effects. Potentially, these correlations, as well as other cuts, can be used for further suppression of missing E_T backgrounds.

Conclusion:

Constraints on the degree of instrumentation of the SBC are not driven by missing E_T physics.

4 Simulation of Muons in the GEM Barrel Calorimeter

Muons in the GEM barrel calorimeter were simulated near η=0 and at η=0.9 using the GEANT package. Details of EM Pb-LKr, hadronic liquid Kr and SBC sections, as well as all dead materials, were included in the calculations. All calorimeter layout parameters were taken from the GEM Baseline 2. The EM section was simulated on the basis of a parallel plate Pb/LKr calorimeter of equivalent thickness.

In our initial simulations, up to ten layers of 50-mm copper followed by 3 mm of scintillator, were used in an instrumented SBC. Figures 31 and 32 show the residual accuracy ($dE = E_{loss} - E_{meas}$) of muon energy-loss reconstruction in the GEM calorimeter at η=0 for 10 instrumented layers and for a non-instrumented SBC, vs the initial muon momentum. Figure 31 corresponds to a perfect momentum resolution of the muon system, while Figure 32 corresponds to the muon system resolution as described in Baseline 2.

Muon energy losses in the EM and hadronic sections of the LKr calorimeter were corrected for assumed measurements in these sections. For the non-instrumented SBC in the right portion of Fig. 31, most of the events lie in the narrow region around the most probable energy loss value while a small fraction of the events experiences large deviations to the right side due to Landau fluctuations (energetic δ electrons) and (at larger energies) due to radiative losses of muons. Since most of the δ electrons contributing to the width of the energy-loss peak near the most probable value in the sampling calorimeter are created inside the absorber and since only a few are measurable in the detecting layers, the energy-loss correction from the measurements in the sampling calorimeter might broaden slightly the narrow peak around the most probable value. On the other hand, large fluctuations due to energetic δ electrons and due to radiative losses will be measured and corrected for with the resolution which is a function of the sampling thickness of the absorber in this portion of the calorimeter.

The residual accuracy of muon reconstruction in Fig. 32 shows that the muon system itself dominates the resolution at the energies above ≈ 50 GeV, though a small fraction of events is measured more adequately with an instrumented SBC.

At the low muon momenta ($E < 50$ GeV) energy measurements in the calorimeter might contribute significantly to the accuracy of the overall muon momentum reconstruction. To simulate this, we have generated, with GEANT, 5000 muons with an energy of 20 GeV near η=0. In this simulation the LKr calorimeter was defined in GEANT as stated earlier and the SBC consisted of 30 layers of 16-mm copper followed by 6 mm of scintillator.

The correlation of muon energy loss in the LKr EM section vs measured energy in this section is shown in Fig. 33. Due to the very fine sampling of the EM section, a very strong correlation is seen in Fig. 33. Correction for the energy measured in this section can be made to an accuracy of $\approx$ 20 MeV, which corresponds to the level of pileup and thermal noise in an EM tower.

A similar distribution for the hadronic LKr section is shown in Fig. 34. Again, a strong correlation is clearly seen. We have tried to use the method employed by the L3 collaboration [7] to minimize the effect of the observed broadening. The calorimetry measurement correction was applied only if the measured energy was above the threshold energy E_{thresh}. Below this threshold, the most probable value was used for the correction. Figure 35 shows, in the lower portion, the deposited energy versus the measured energy in the LKr HC, together with the projection on the $E_{measured}$ axis. The upper portion shows the contribution to the muon P_t resolution and to the muon inefficiency beyond 1.5σ of combined muon system and calorimeter resolution as a function of the E_{thresh} parameter. Optimum E_{thresh} corresponding to the broad region between 50 and 85 MeV of energy deposited in LKr suggests that the calorimeter correction can be used without regard to E_{thresh}. Nevertheless, for the next analysis, the parameter E_{thresh} for the liquid hadron section was fixed at 80 MeV.

In Figs. 36 and 37 a similar analysis is presented for the SBC section with different number of scintillator readout layers. The best resolution and efficiency levels achieved in an analysis with a 6 λ liquid calorimeter are shown in the upper plots by the dotted line. To preserve the best resolution and efficiency, a SBC with 20-30 scintillator layers should be chosen, although even with 4 scintillator layers, the global resolution for muon energy reconstruction at 20 GeV is only 10-12% worse than with 30 readout layers. The corresponding inefficiency increases from 4 to 10%. Of course, at higher muon energies this difference becomes negligible.

Contributions to the muon P_t resolution from calorimeter and muon system measurements are shown in Figs. 38 and 39 for η=0 and η=0.9 as a function of muon P_t. The two series of points are for a 6 λ liquid calorimeter (stars) and for a 10.5 λ calorimeter (triangles). The latter calorimeter consists of a 6 λ LKr section followed by a 4.5 λ SBC, instrumented with 4 scintillator layers. An open star in Fig. 38 depicts the RD3 result for a 6 λ noble-liquid calorimeter, measured with 180 GeV muons. The fact that the RD3 result is slightly worse than the one obtained in our simulations for the 6 λ LKr GEM calorimeter is likely due to the larger noise contribution in RD3.

Muon inefficiencies as a function of muon momentum are shown in Figs. 40 and 41 for 6 λ and 10.5 λ calorimeters, as described above.

We can conclude that the design of a SBC with 4 readout layers, as optimized for the detection of hadronic jets in GEM, provides a measurement of muon momenta which is only slightly worse at low energies (below 40-50 GeV) than a SBC with perfect sampling (30 readout layers) would have provided. At higher energies (above 40-50 GeV), the SBC design with 4 readout layers does not affect the correction for muon energy loss in the calorimeter. It should be pointed out that at muon momenta less that 20-30 GeV, a poorly instrumented SBC will strongly affect the muon inefficiency.

5 Light Collection Simulations of SBC Readout

Extensive research of the scintillating tile technique with WLS fiber readout has been performed by SDC and CDF collaborations [8]. At CEBAF, tile/fiber studies have been done for the CLAS detector [9]. In the design of the GEM SBC detector, the experience gained by these collaborations can be used. A summary of the discussions held at FNAL and CEBAF is given in [10].

The LTRANS code [11, 12] was used in our simulations to optimize the design geometry and readout of scintillator/fibers in the GEM SBC. This code takes into account the following processes:

1. Ionization losses in media (dE/dx);
2. Scintillator efficiency (dN_γ/dE);

3. Spectral dependence of emitted light;
4. Up to 3 components of emitted light with different weights and emission time constants;
5. Spectral light absorption in different media;
6. Spectral light reemission in WLS fiber;
7. Spectral absorption at different surfaces;
8. Secular and diffuse spectral reflection at painted and mirror surfaces;
9. Reflection/refraction at the boundary of two transparent media;
10. Spectral light propagation along WLS and clear fibers;
11. Spectral response of PMT photocathodes; and
12. Time development of light propagation.

Different geometrical objects (boxes, cylinders, toroids, etc.) are available in the code to describe the tile/fiber configurations. The data base of the code contains spectral data for scintillators, WLS, and clear fibers, diffuse and mirror coatings, and spectral quantum efficiencies of the photocathodes.

The code has been benchmarked by the simulation of the CEBAF setup [9]: the BC-408 scintillator of 200 * 10 * 1 cm^3 size with 5 embedded BCF-91A WLS fibers of 2-mm diameter and 2.5-m length, measured with a source position at 2 m from the photocathode, with fibers not glued in grooves, and with far ends of the WLS fibers blackened. The response measured by CEBAF is 5.6 p.e./MeV. Our MC simulations gives 5.5 p.e./MeV. For glued fibers the agreement is also very reasonable: CEBAF gives a glued/not-glued factor of 1.85 while our MC simulation predicts a factor of 1.89. Experimental numbers have an accuracy of 10%, and the systematic error of the Monte Carlo calculations is determined mainly by the assumptions regarding the optical properties of the components.

For GEM SBC simulations, the following components have been selected:

1. Plastic scintillator BC-412:
   - light output: 60% of anthracene

- decay time: 3.3 ns
- refraction index: 1.58
- light attenuation length: 50 cm
- light emission spectrum: see Fig. 42

2. WLS fiber BCF-91A (400 ppm dye concentration):
    - decay time: 12 ns
    - core refraction index: 1.60
    - cladding refraction index: 1.49
    - light attenuation length: see Fig. 42
    - light emission spectrum: see Fig. 42
3. Clear fiber BCF-98:
    - core refraction index: 1.60
    - cladding refraction index: 1.49
    - light attenuation length: see Fig. 42
4. The green extended photocathode was used as a photodetector with a quantum efficiency 66 mA/W at 525 nm.

The following are major requirements of the GEM SBC detector:

- reliable detection of MIP in 4 SBC layers forming one readout tower
- time rms resolution < 5 nanoseconds
- response uniformity within one tile < 10%
- tile to tile uniformity < 10%

In our simulations we have tried to address the following questions which are relevant to the design of the GEM SBC detector:

- How many WLS fibers per given size tile should be used?

- What should be the scintillator thickness and fiber diameter and length?

- What is the effect of the mirroring of the free fiber end?

- Should the fibers be glued in the tile grooves?

- What reflective materials should be used for tile wrapping?

We have tried to give an answer to these questions by simulation of total light yield, timing and uniformity of the tile/fiber optical assemblies. Two basic tile/fiber configurations (shown in Fig. 43) were considered: fibers embedded in the sides (configuration #1) or fibers embedded in the flat top (configuration #2) of the tiles. The quality of the groove inner surfaces was assumed to be optically perfect.

Some typical results of these simulations are presented in Table 3 and in Fig. 44 - Fig. 47. One can see from the Table 3 that the top configuration of the fibers is more effective than the side one. This configuration also gives a smaller transverse response nonuniformity and involves simpler machining. Another advantage of the fiber-top configuration is that it allows a variation in the number of fibers per tile from 1 to several, in order to optimize uniformity and light yield. In further discussion we consider only the top (#2) configuration of the fibers, unless stated otherwise. Figure 44 shows the simulated number of photons transported to the photocathode versus the tile thickness. The arrow indicates the recommended tile thickness of 6 mm. In Fig. 45 the efficiency of light transport (to the photocathode) is shown as function of fiber diameter. The arrow indicates the 1-mm diameter chosen for the practical reasons. Figure 46 shows how the efficiency depends on the number of fibers per tile. The arrow indicates 2 fibers per tile configuration. The transverse distribution of tile response with 2 glued in fibers is shown in Fig. 47. The rms is equal to 2.8% and the peak-to-peak variation is 10%. The ratio of responses for glued and non-glued fibers is equal to approximately 2 and is the same for the both configurations shown in Fig. 43. This result is qualitatively in agreement with measurements made at CEBAF [9] regarding the effect of fiber glueing.

Comparisons of different materials used for wrapping is shown in Table 4. It contains relative efficiencies and transverse response nonuniformities for a tile of 50 * 9 * 0.6 cm^3 size with 2 fibers glued in the grooves. All reflectors were assumed to have no optical contact with the tile. Thus, some fraction of the light was always transported due to the total reflection inside the tile. The reflection quality of the aluminized mylar may be not perfect as compared to an ideal Al mirror. We calculated the aluminized mylar wrapping effect assuming different reflection efficiencies relative to an ideal Al mirror. One can see that the wrapping with a white diffuse material (c.f. Tyvek [14]) is almost as effective as perfect aluminized mylar. It is also clear from these data that about 30% of the light collected results from total internal reflection inside the tile.

Values of the product of WLS fiber light capture efficiency and transport efficiency for mirrored and nonmirrored WLS fibers, for different lengths of WLS and for clear fibers are summarized in Table 5. The quantum efficiency of the WLS reemission is assumed to be 100%. (According to Ref. [13], the reemission efficiency of the WLS is ~ 85%.) The mirroring of the rear end of the WLS fiber gives the advantage of higher efficiency and of better response uniformity. The increase in WLS fiber length (up to 65 cm for the 50-cm-long tile) helps to filter out shorter wave length components and thus improves the longitudinal nonuniformity. Further length increase does not improve the response uniformity, but reduces the efficiency. The clear fiber length variation in the range 100 - 500 cm results in a 20% variation of transport efficiency.

In order to check the advantages of an extended green photocathode, the calculation of photocathode efficiency to the light emitted by the WLS fiber and transported along the clear fiber has been made for standard bialkali, extended green, and trialkali photocathodes. The results are shown in Table 6. The green extended photocathode and the trialkali photocathode have almost twice the efficiency of the standard bialkali photocathode.

For the chosen 6-mm tile thickness, a more detailed analysis has been made. The number of photoelectrons and the dependence of the efficiency on the threshold have been simulated for 50 GeV/c muons (obtained through GEANT) crossing 4 layers of tiles, with each layer being placed between 13 cm of copper absorber. The WLS fiber was connected to a 5-m-long clear transport fiber. The photomultiplier with a green extended photocathode was used. Distributions of numbers of photoelectrons for different fiber numbers and for diameter configurations are shown in Figs. 48 - 51. Efficiency vs threshold is shown at Fig. 52. Results for average response values, arrival r.m.s. times, and nonuniformity of the response over the tile surface are presented in Table 7. The most probable value of the muon response (26.9 p.e. for 2 fibers per tile with no glue) seems to be satisfactory for the required SBC performance.

References

[1] GEM Collaboration, *Letter of Intent,* GEM TN-92-49 (1991).

[2] K. Shmakov, *Missing E_T in Jets Due to Leakages into Scintillator Barrel Calorimeter,* GEM TN-93-295 (1993).

[3] F. E. Paige and A. V. Vanyashin, *Effects of Limited Calorimeter Coverage on E_T^{miss}*, GEM TN-92-70 (1992).

[4] GEM Collaboration, *Progress Report on the GEM Detector Baseline Design,* GEM TN 92-231 (1992).

[5] B. Moore, *CALOR89 Calculations for the GEM LKr Barrel Calorimeter,* GEM TN 93-383.

[6] *GEM Baseline 2.*

[7] R. Y. Zhu, private communication.

[8] *"R&D results on scintillating tile/fiber calorimetry for the CDF and SDC detectors"*, Nucl. Instrum. Methods Phys. Res. A315 (1992) 317-321.

[9] *"Embedded Waveshifting Fiber Readout of Long Scintillators"*, Contribution to the III International Conference on Calorimetry in High Energy Physics, Sept. 29 - Oct. 2, 1992 Corpus Christi, Texas.

[10] *Scintillating Tiles Production and Light Readout*, GEM TN-93-305, March 1993.

[11] A. Savin, K. Shmakov, E. Shoumilov, V. Shoutko, E. Tarkovsky, *The LTRANS code* (in preparation).

[12] *Liquid Scintillator Calorimetry*, A Research and Development Proposal Submitted to SSCL by LLNL, UMiss, ORNL, UT, TIFR, ITEP, IHEP; September 1991.

[13] C. R. Hurlbut, Bicron Corp., Private communication.

[14] Type 1073D Tyvek, DuPont Fibers, Chestnut Run Plaza, P.O. Box 80705, Wilmington, DE 19880.

List of Tables

List of Figures

Inner radius of the system	2923 mm
Outer radius of the system	3702 mm
Z-extent of absorber	4890 mm
Total z-extent (including readout)	5640 mm
Number of absorption lengths at 90 degree	4.01λ
Number of mechanical modules ($\varphi * \Theta$)	22 x 2 = 44
Total weight (SS support and modules)	1372 Mg
Weight of outer SS support tube	201 Mg
Weight of outer barrel passive absorber	223 Mg
Weight of 44 modules	948 Mg
Weight of the largest (smallest) module	24(8) Mg
Thickness of scintillator/copper stack	565 mm
Thickness of copper layers	128.6 mm
Number of scintillator layers	4
Gap in the absorber for scintillator	12 mm
Thickness of scintillator tiles	6 mm
Total number of readout/PMT channels	640
η coverage	±1.28
angular coverage	31-149°

Table 1: *Characteristics and parameters of the Scintillating Barrel Calorimeter.*

Number of layers in SBC	best(worst) layer number	best(worst) constant term %
0 (non-instrumented SBC)	- -	4.77±0.14
1	5 (1 or 10)	4.06±0.13 (4.47±0.15)
2	3, 9 (8, 10)	3.84±0.14 (4.41±0.15)
3	3,6,9 (6,7,8)	3.69±0.13 (4.39±0.14)
4	2,4,6,9 (7,8,9,10)	3.69±0.13 (4.39±0.14)
10	-	3.75±0.13

Table 2: *Optimum layer distribution vs layer position.*

Geometry description	Glue in grooves	Efficiency (%)	Transversal nonuniformity R.M.S.(%)
tile: 50 * 9 * 0.6 cm^3, configuration # 1	yes	1.10	7.5
tile: 50 * 9 * 0.6 cm^3, configuration # 1	no	0.60	12.8
tile: 50 * 9 * 0.6 cm^3, 2 fibers in configuration # 2	yes	1.18	2.8
tile: 50 * 9 * 0.6 cm^3, 2 fibers in configuration # 2	no	0.56	7.3
tile: 50 * 9 * 0.6 cm^3, 1 fiber in configuration # 2	yes	0.77	5.0

Table 3: *Light collection efficiency for different tile/fiber configurations.*

Wrapping	Efficiency $(x10^{-2})$	Transversal nonuniformity R.M.S.(%)
perfect aluminized mylar with 100% efficiency	1.18	2.8
aluminized mylar with 80% efficiency	0.92	3.6
aluminized mylar with 60% efficiency	0.76	4.0
aluminized mylar with 40% efficiency	0.64	3.8
aluminized mylar with 20% efficiency	0.54	3.8
aluminized mylar with 0% efficiency	0.45	2.7
white diffuse wrapping	1.16	4.5

Table 4: *Light collection efficiency for different tile wrappings. Tile size: 50 * 9 * 0.6* cm^3*, 2 WLS fibers of 1-mm diameter glued in the grooves at the top of the tile. Clear fiber length is 100 cm.*

Al mirror at the WLS fiber far end	WLS fiber length (cm)	Clear fiber length (cm)	$\epsilon_{WLSF}{}^{*}\epsilon_{tr}$ (%)	Longitudinal nonuniformity R.M.S.(%)
no	50	100	2.35	18.4
yes	50	100	3.58	7.0
no	65	100	2.06	12.6
yes	65	100	3.10	4.7
yes	65	200	2.91	4.3
yes	65	300	2.77	4.2
yes	65	400	2.61	4.0
yes	65	500	2.47	4.0
no	80	100	1.78	9.9
yes	80	100	2.76	3.7

Table 5: *WLS and transport fibers efficiency* $\epsilon_{WLSF}{}^{*}\epsilon_{tr}$ *for different WLS and clear transport fiber lengths. Tile length: 50 cm.*

Photocathode	Average quantum efficiency (%)
standard bialkali	6.6
green extended	12.3
trialkali	12.6

Table 6: *Comparison of calculated quantum efficiencies of different photocathodes for the light emitted by WLS fiber of 65-cm length. Fiber glued in a tile of 50 * 9 * 0.6* cm^3 *size wrapped with perfect aluminized mylar; light is transported along the 100-cm-long clear fiber. Fiber diameters are 1 mm.*

Tile/fiber geometry	Average response (p.e./μ)	Arrival time r.m.s. (ns) (threshold 4 p.e.)	Total response nonuniformity (%)
1 fiber 1-mm dia glued in	44.3	1.6	7.6
2 fibers 1-mm dia glued in	77.5	1.4	4.5
1 fiber 2-mm dia glued in	79.5	1.1	7.4
2 fibers 1-mm dia not glued in	26.9	1.9	9.7

Table 7: *Results of simulation of 4 layer tower response to 50 GeV muons for different tile/fiber geometries. Tile size: 50 * 9 * 0.6 cm*^{3}. *WLS fiber length: 65 cm. Clear fiber length: 5 m.* $< \Delta E_\mu > = 6.4$ *MeV.*

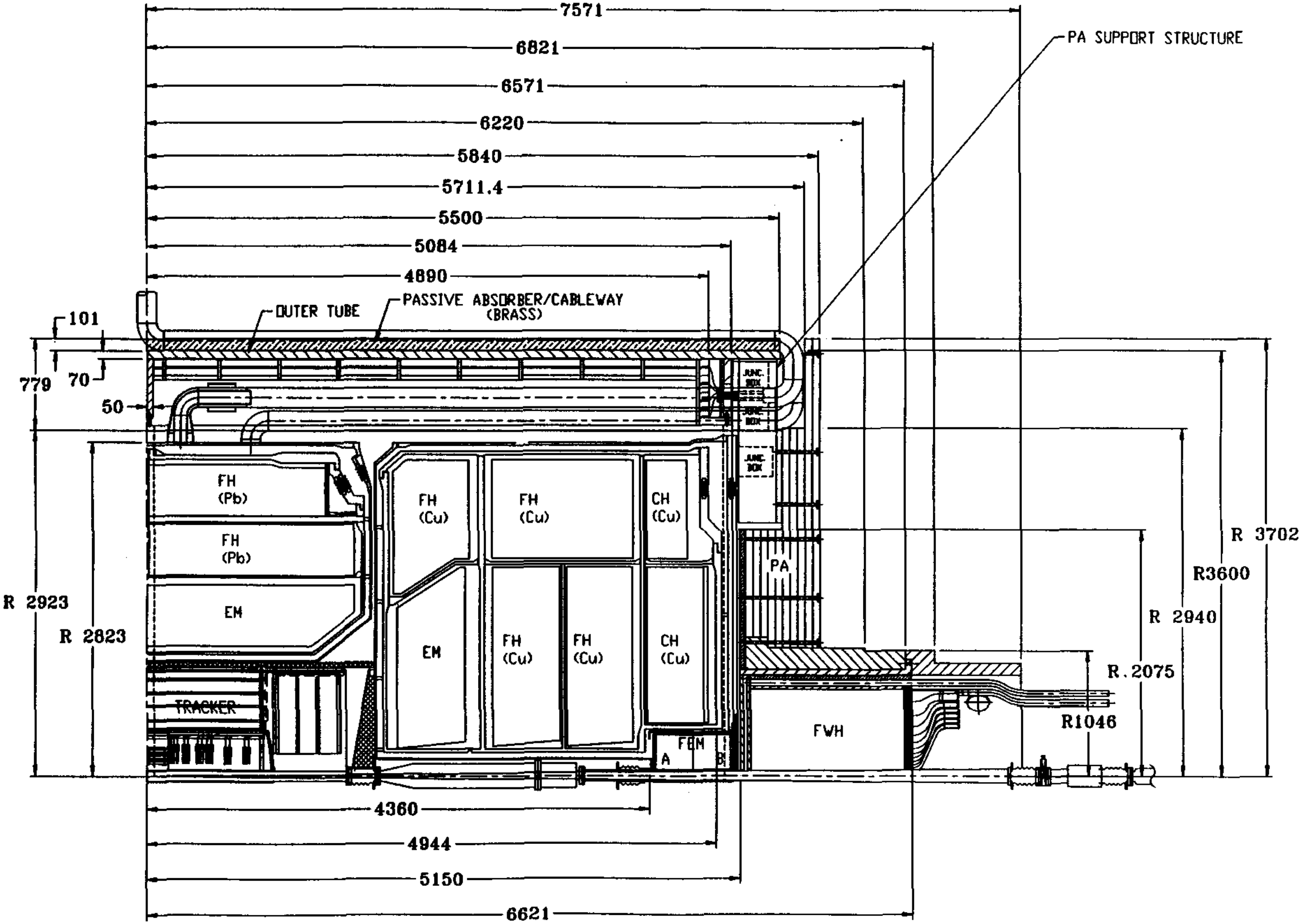

Figure 1: *GEM Calorimeter overview.*

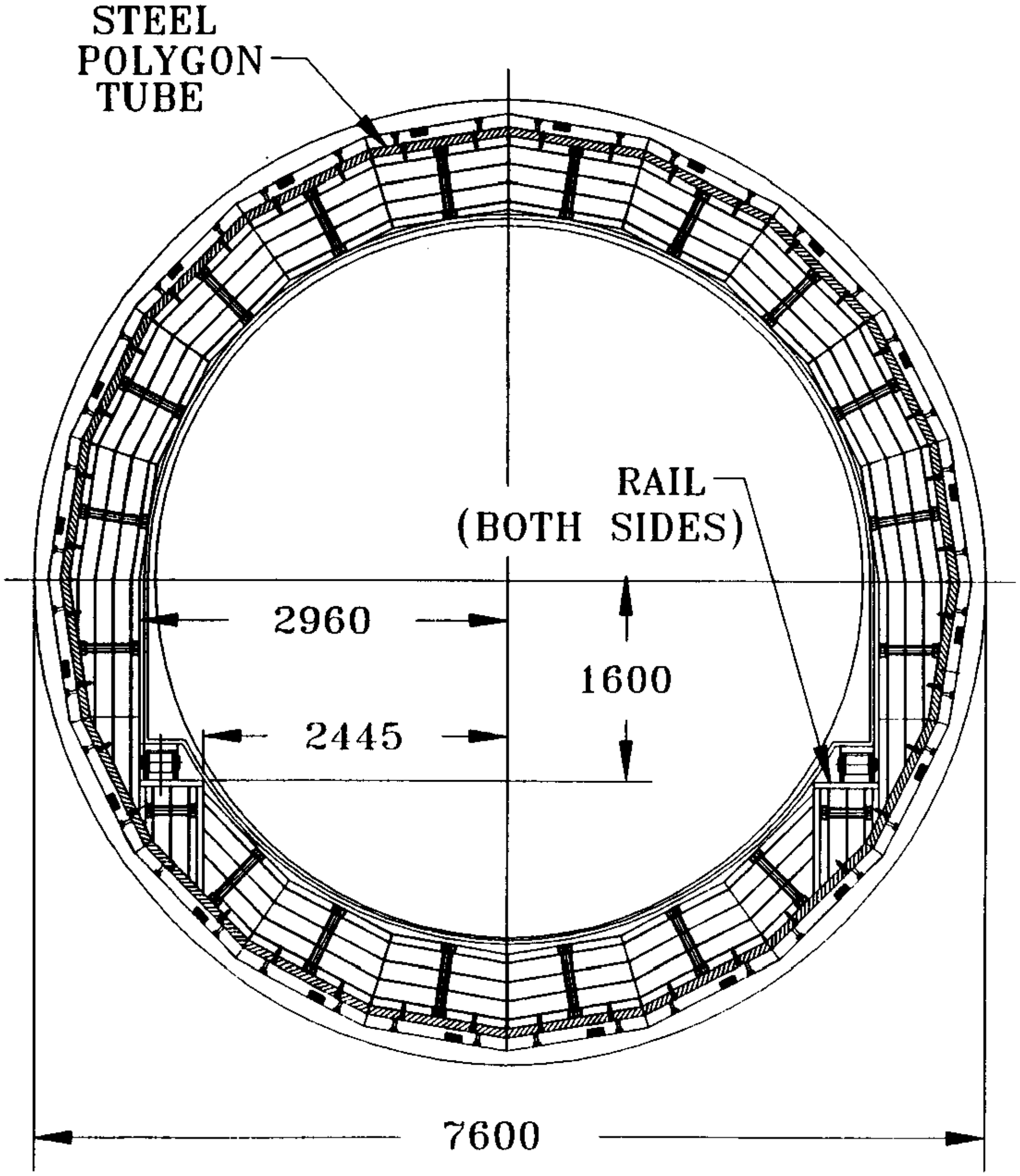

Figure 2: *Scintillating Barrel Calorimeter, radial view.*

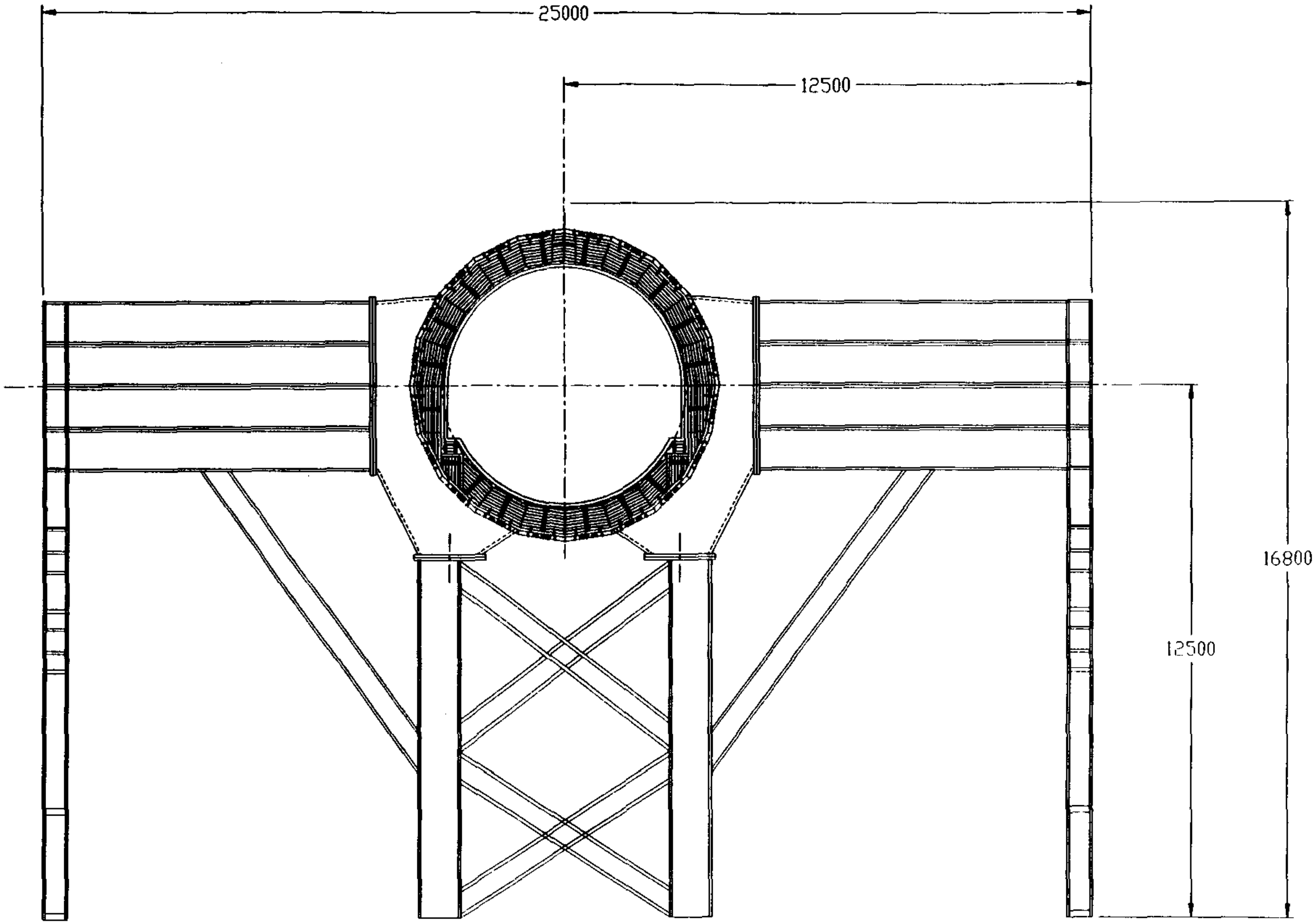

Figure 3: *Central Detector Support (CDS), outer support tube and modules of Scintillating Barrel Calorimeter are shown.*

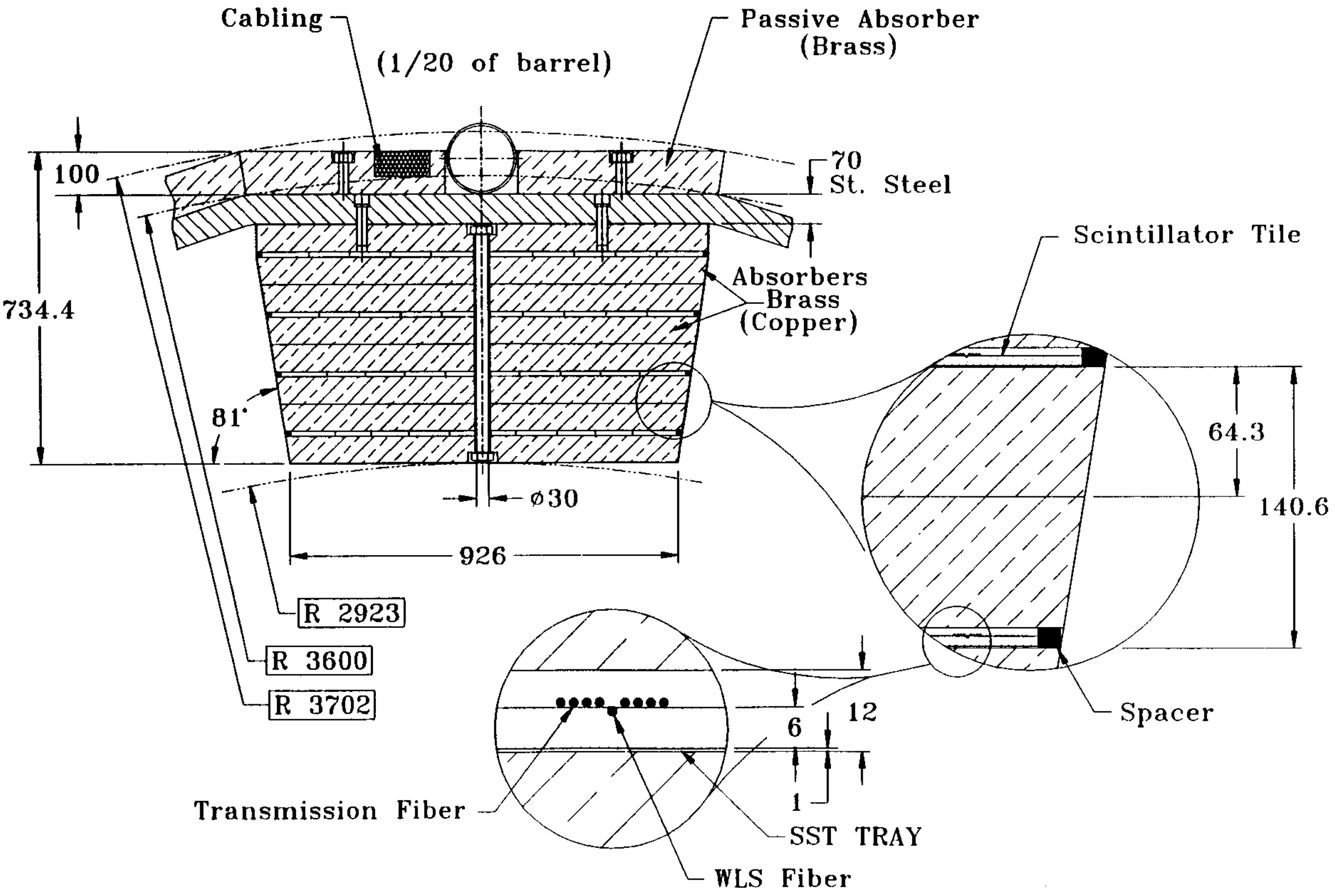

Figure 4: *Structural view of one module of Scintillating Barrel Calorimeter.*

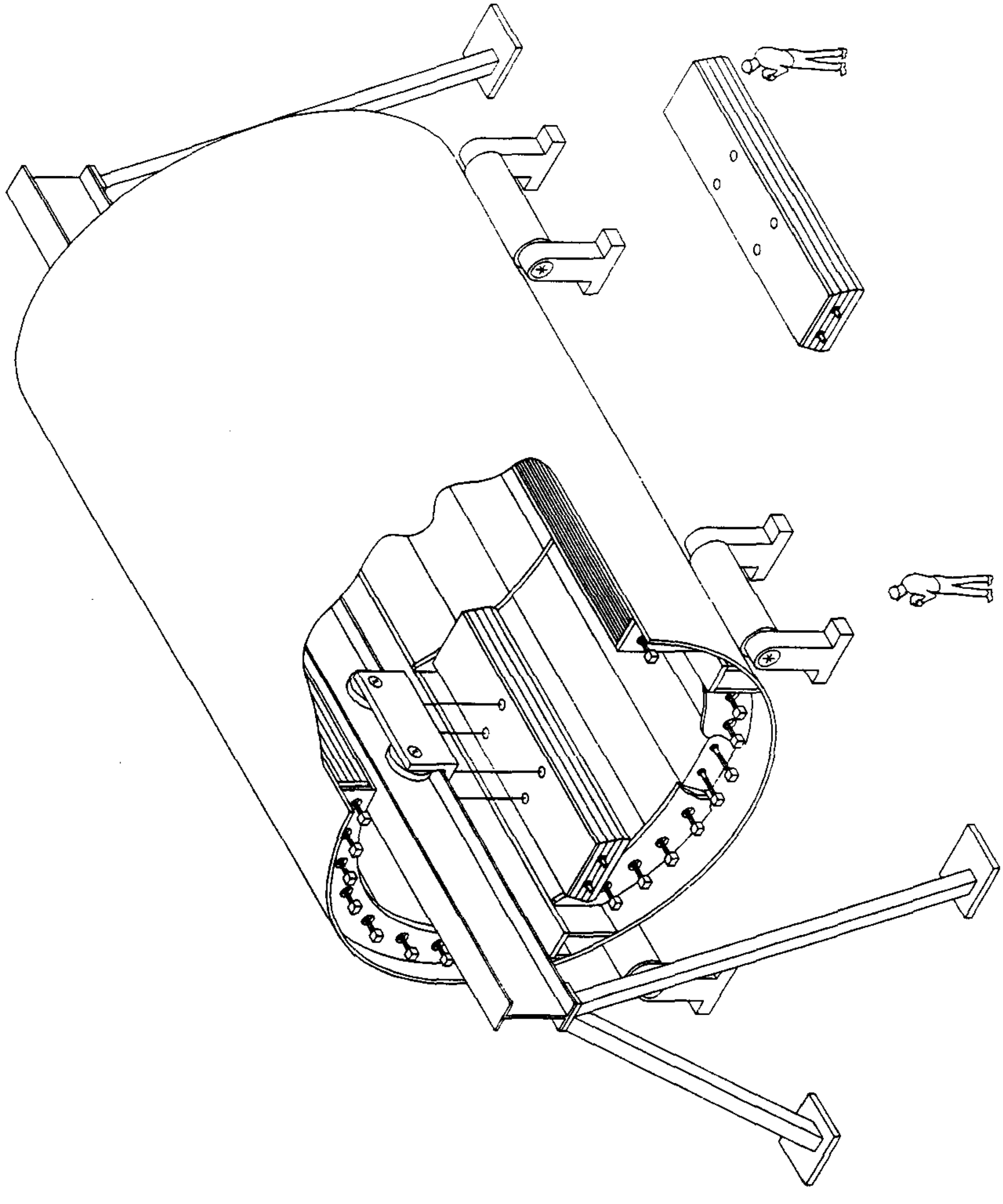

Figure 5: *Modular construction of Scintillating Barrel Calorimeter.*

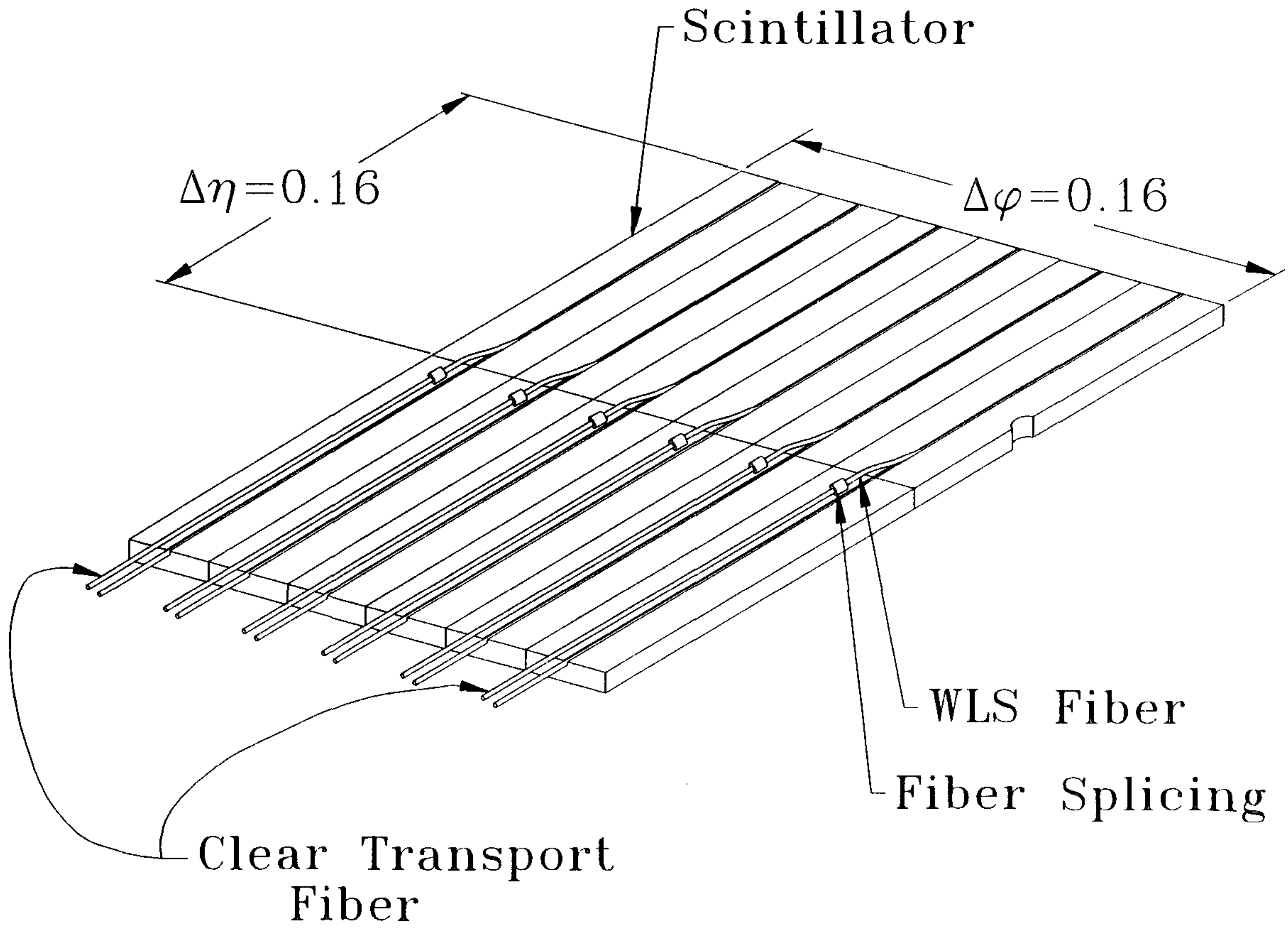

Figure 6: *The scintillating layers with WLS fibers and clear transport fibers.*

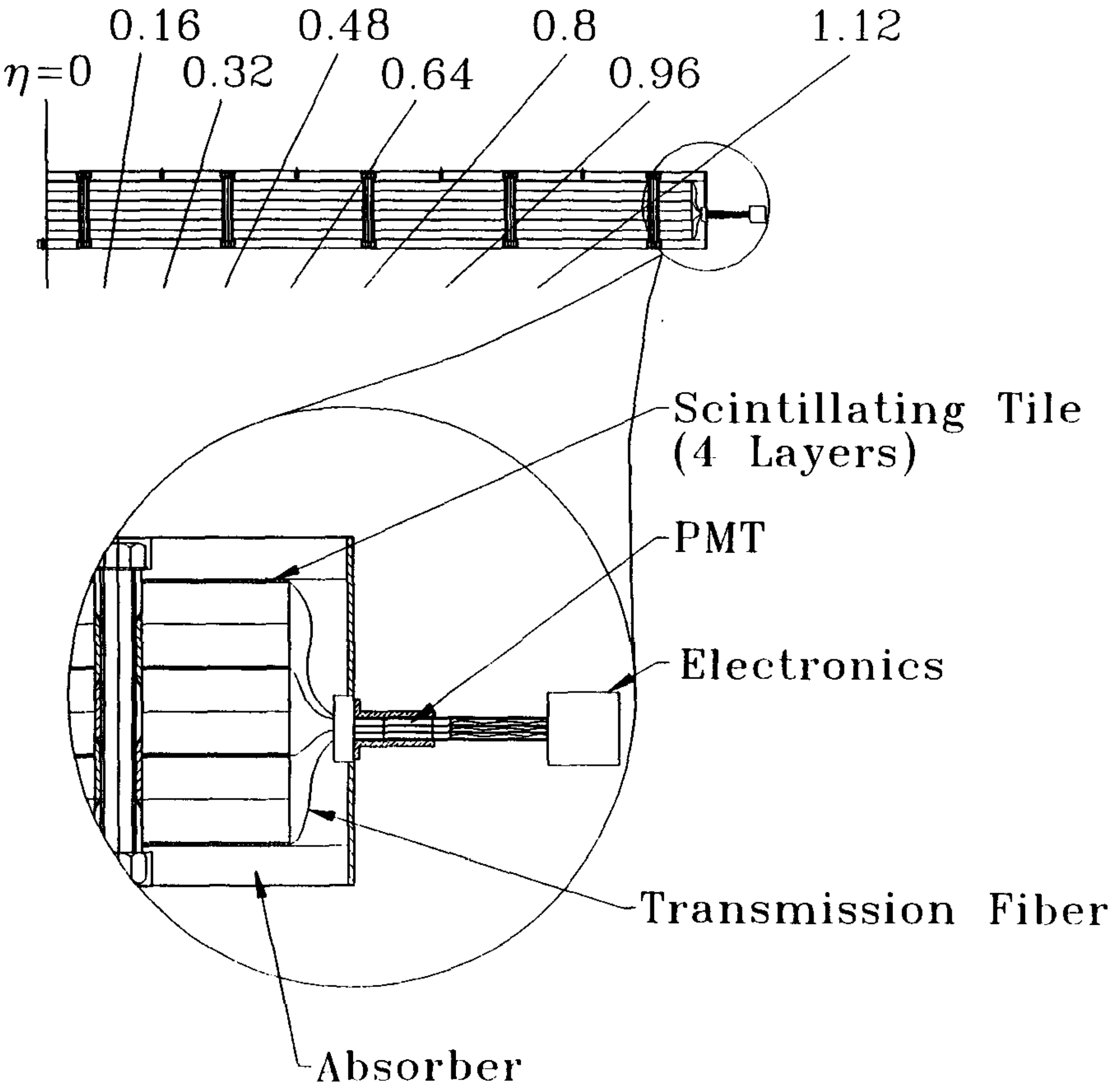

Figure 7: *Fibers from 4 layers within one 0.16 * 0.16 tower, or total 24 tiles, are read out by one photomultiplier tube.*

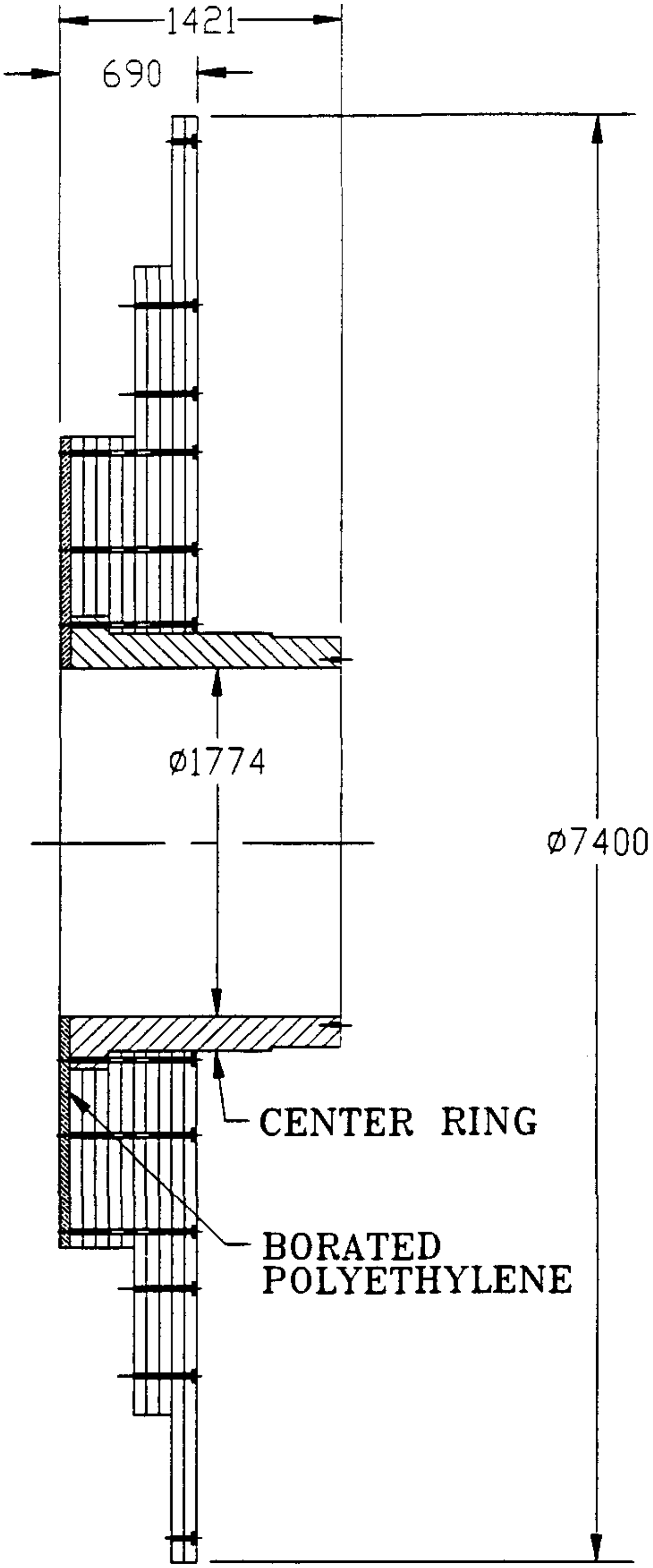

Figure 8: *The Passive Absorber assembly.*

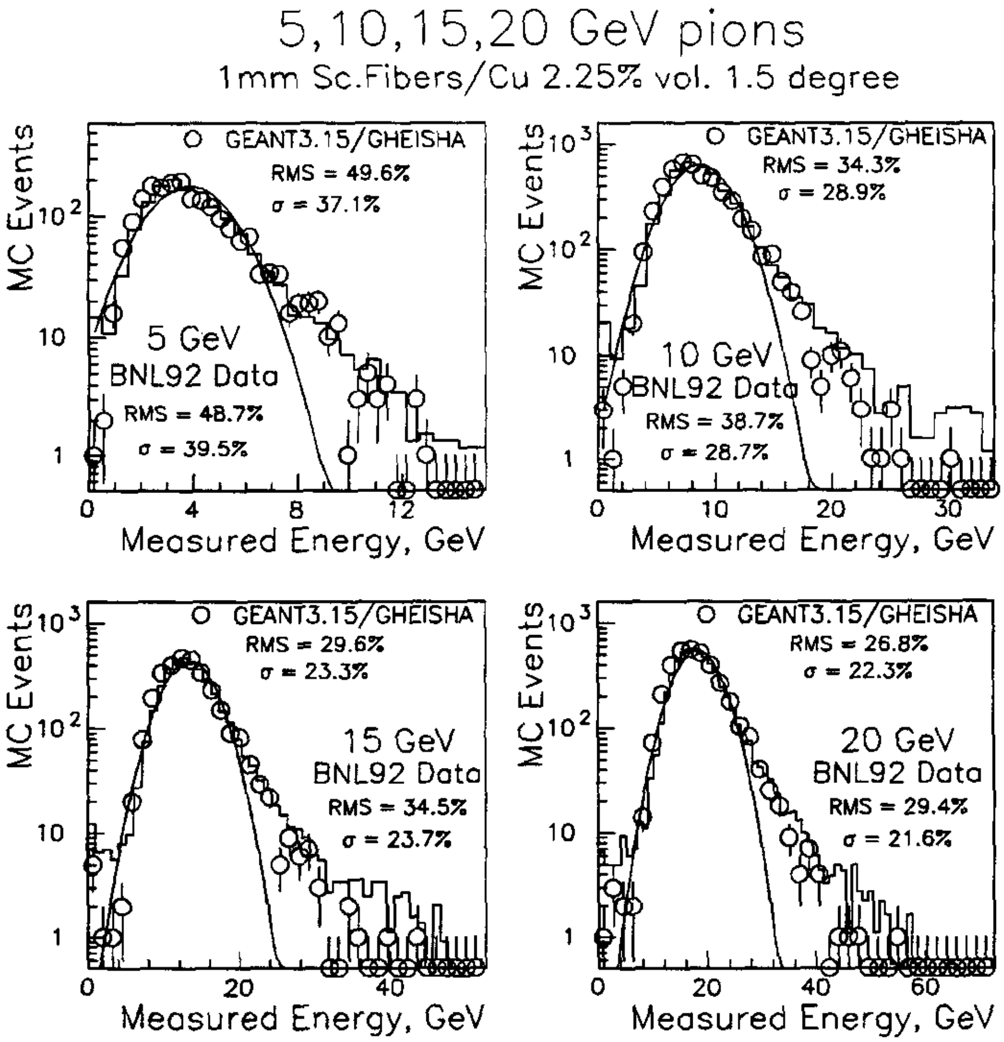

Figure 9: ***Comparison of MC results with BNL-92 beam test data.***

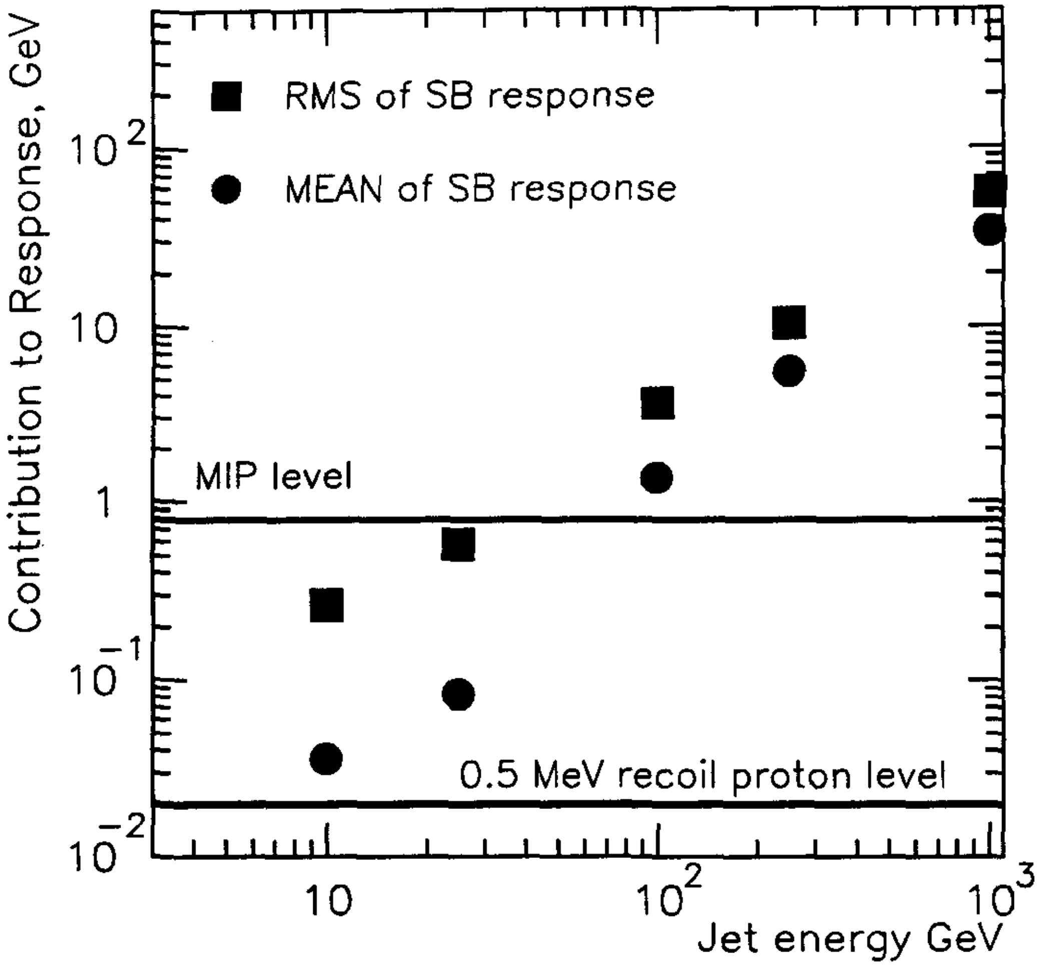

Figure 10: *SBC response (MEAN and RMS) vs jet energy. MIP and "neutron" levels are shown.*

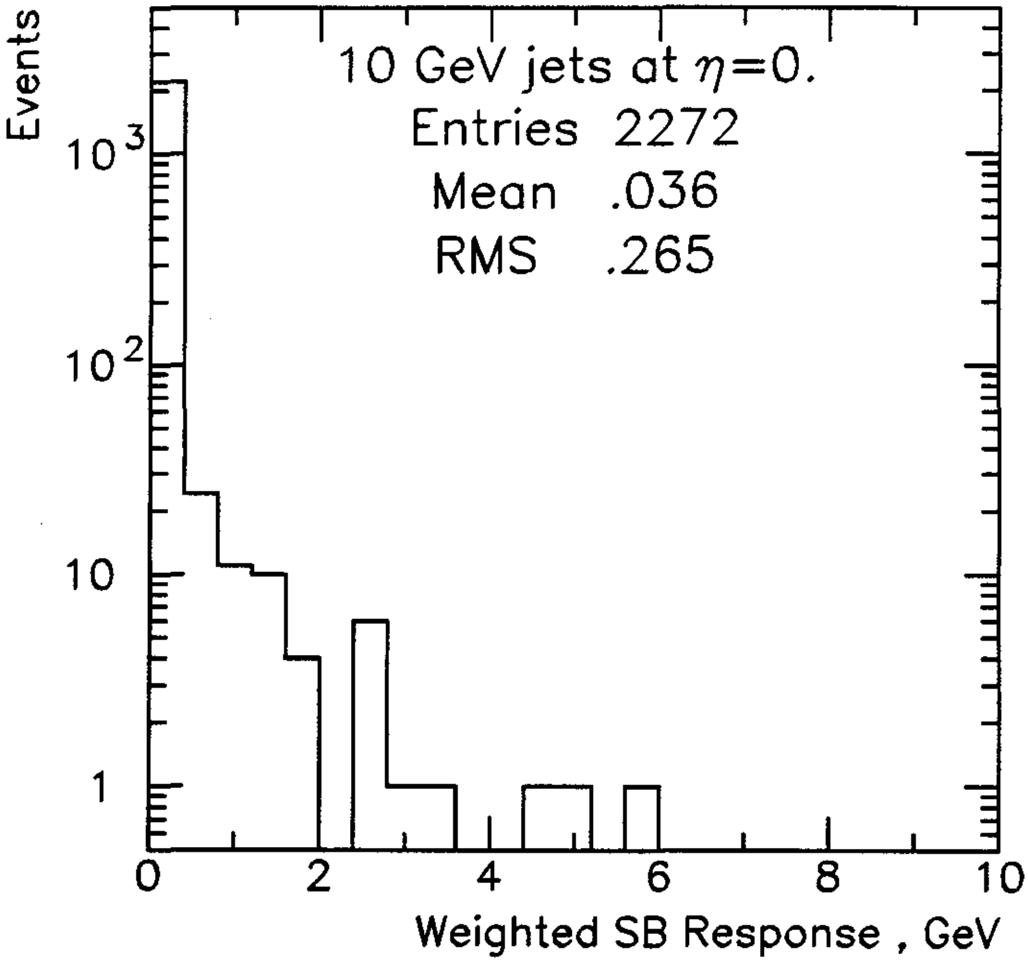

Figure 11: *SBC response for 10 GeV jets.*

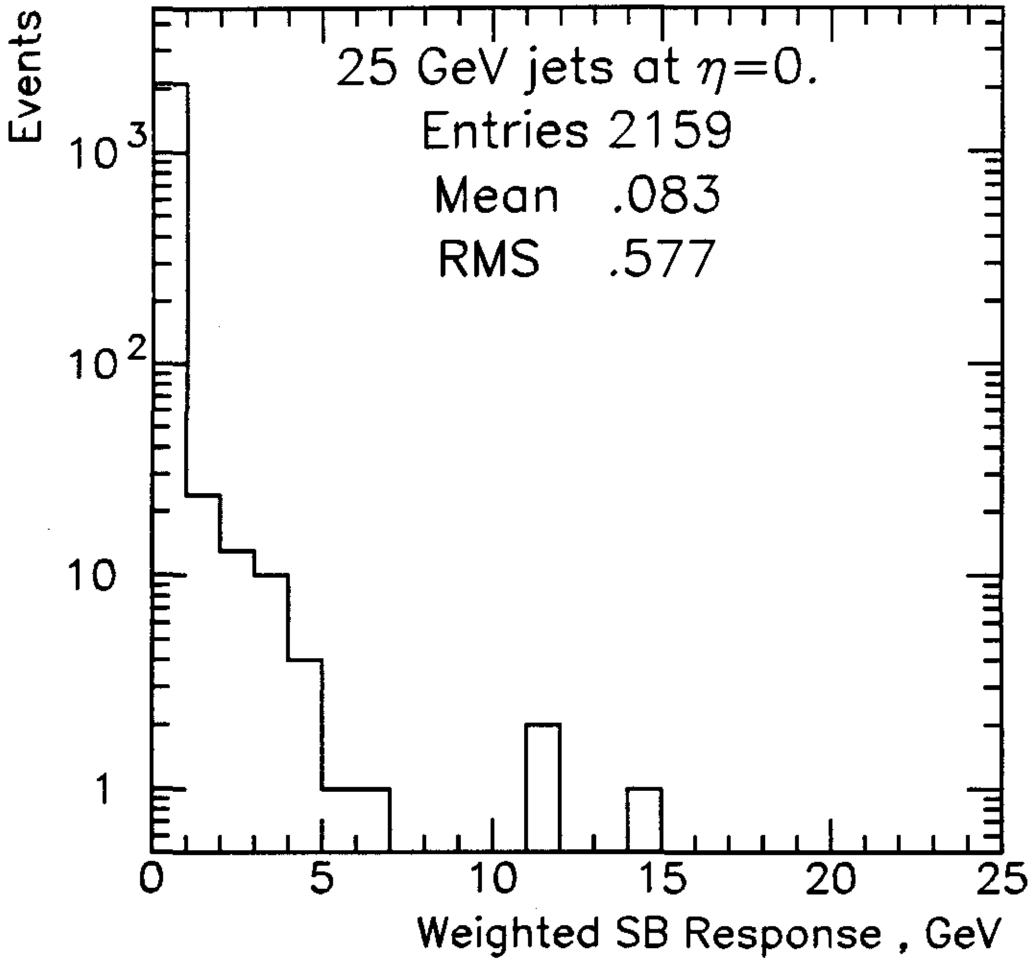

Figure 12: *SBC response for 25 GeV jets.*

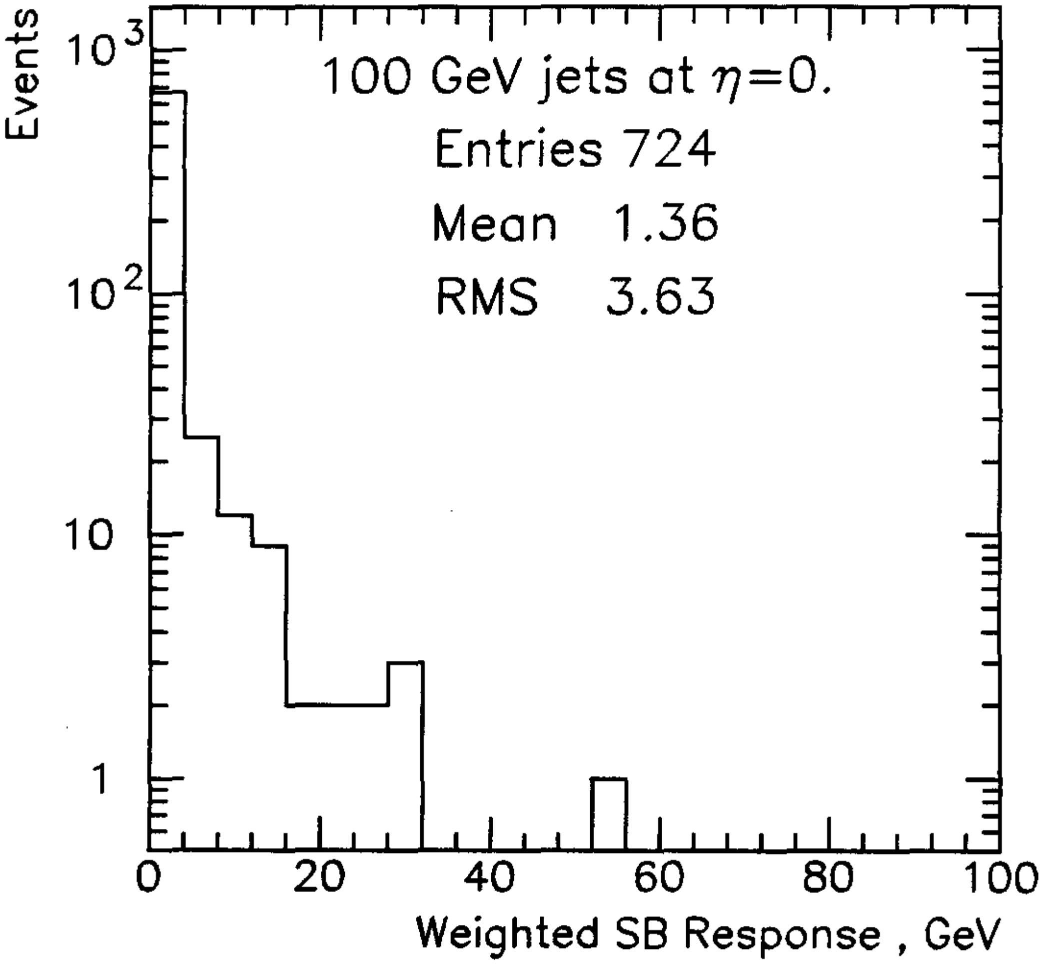

Figure 13: *SBC response for 100 GeV jets.*

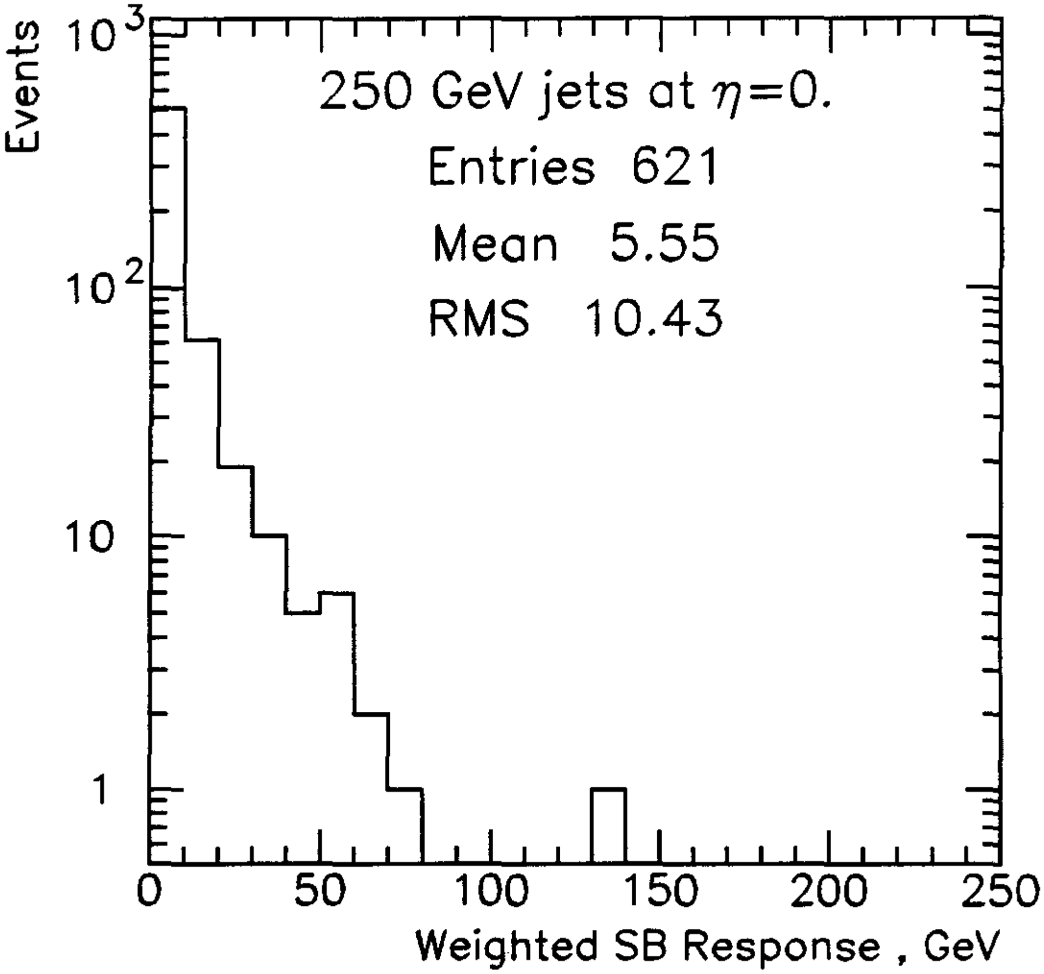

Figure 14: *SBC response for 250 GeV jets.*

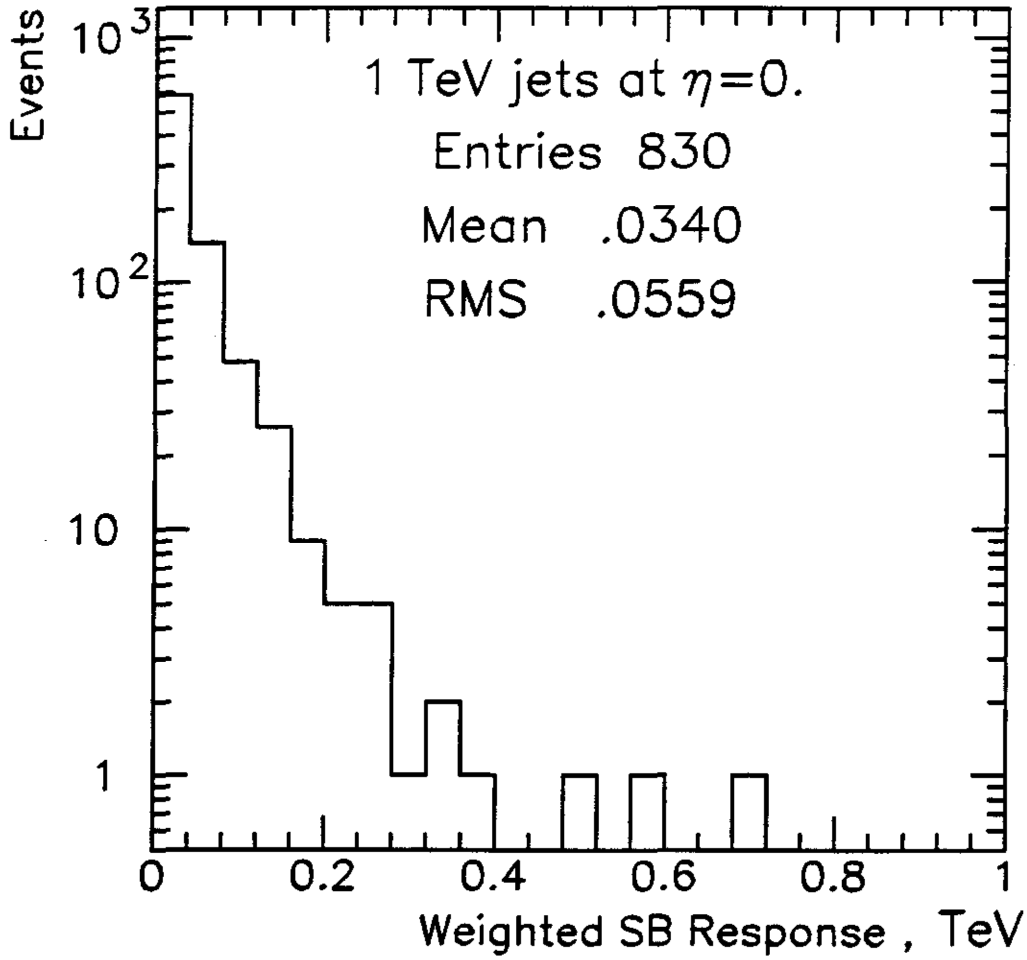

Figure 15: *SBC response for 1 TeV jets.*

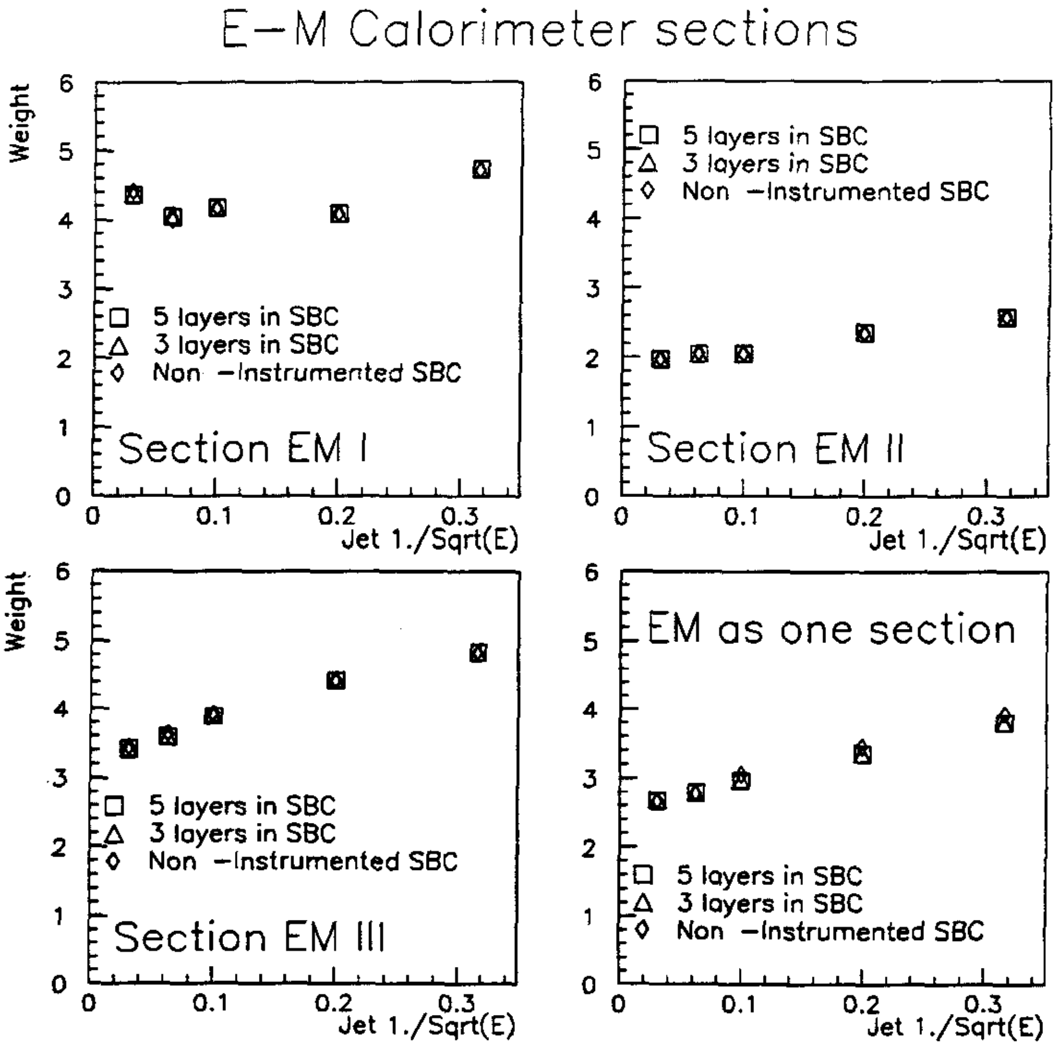

Figure 16: *Weights for EM sections.*

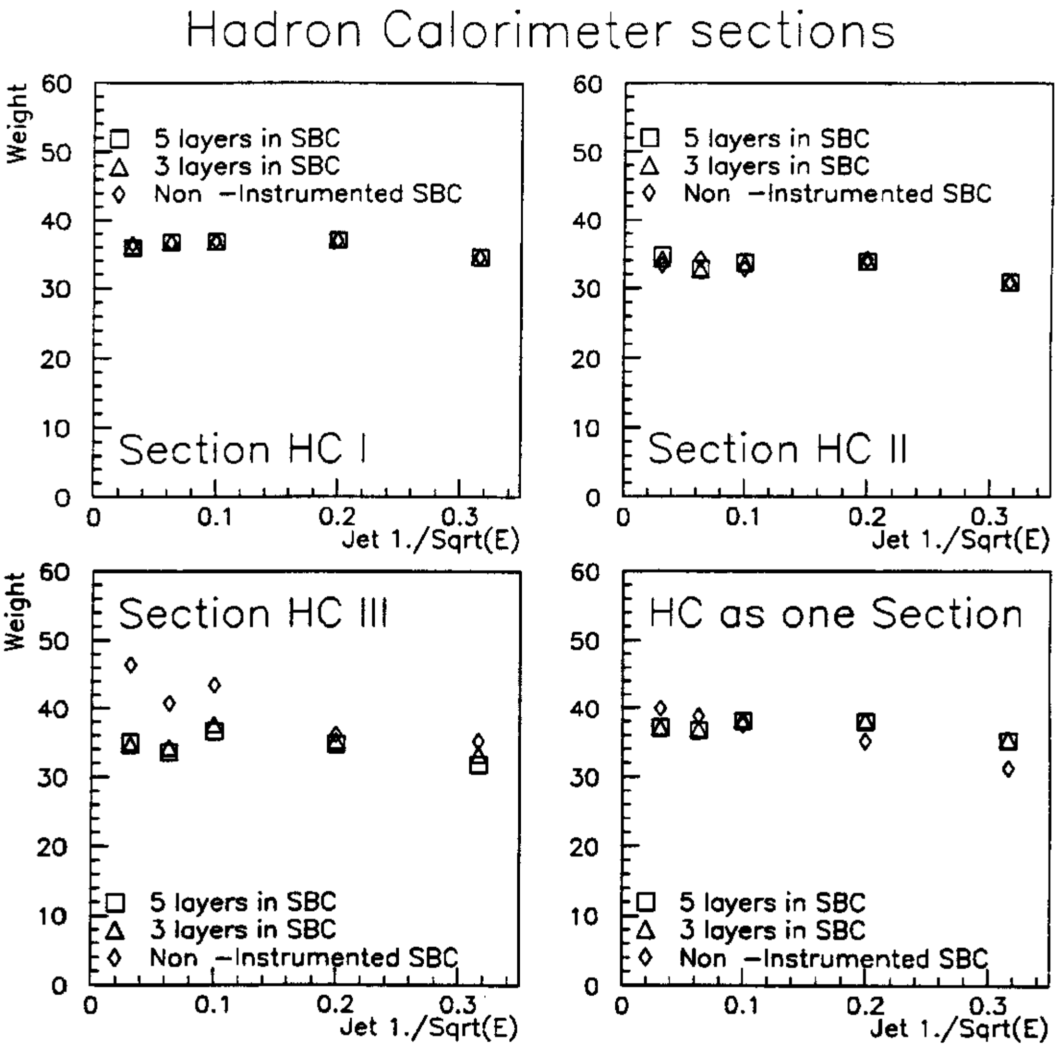

Figure 17: ***Weights for HC sections.***

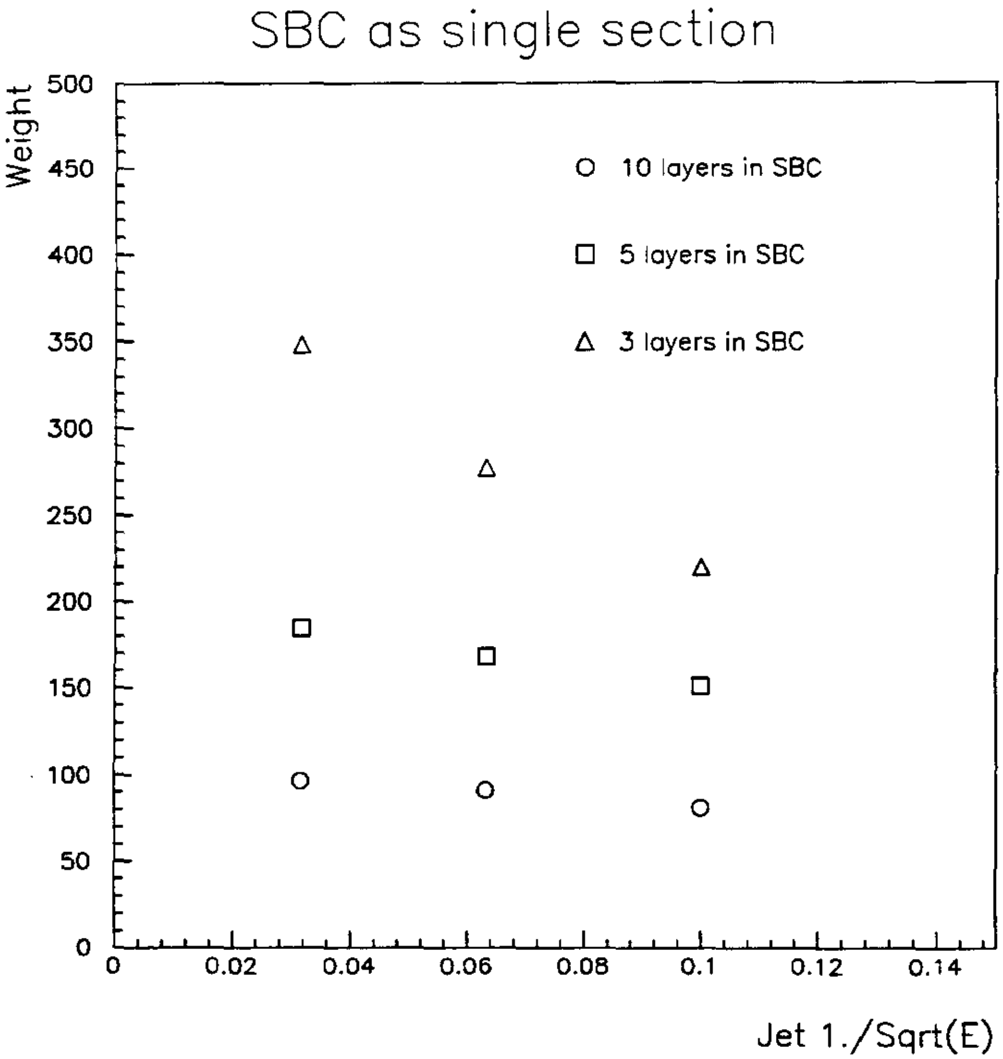

Figure 18: ***Weights for Scintillating Barrel Calorimeter.***

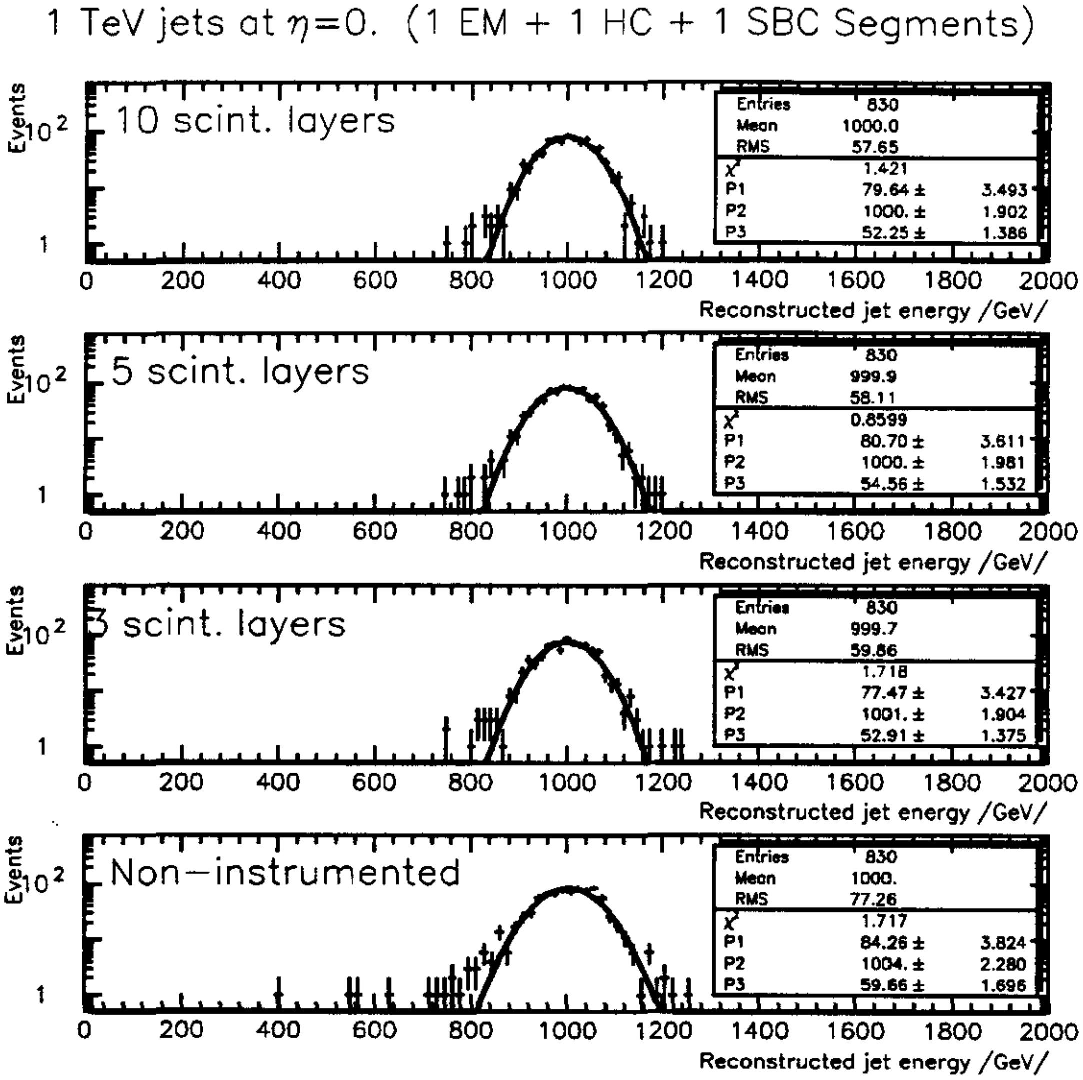

Figure 19: *EM + HC + SBC response spectrum for 1 TeV jet (no segmentation in EM and HC).*

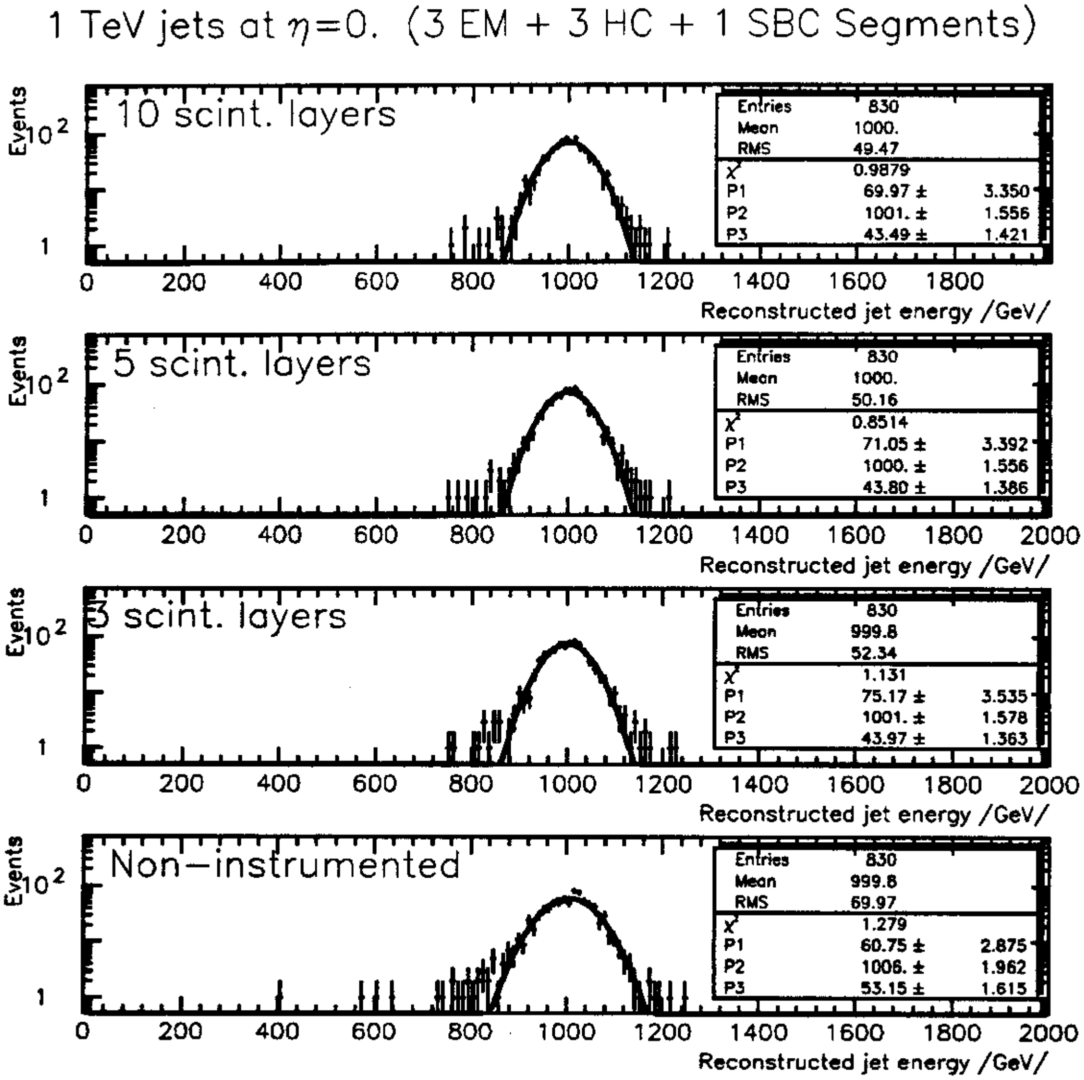

Figure 20: *EM + HC + SBC response spectrum for 1 TeV jet (3 segments in EM and 3 in HC).*

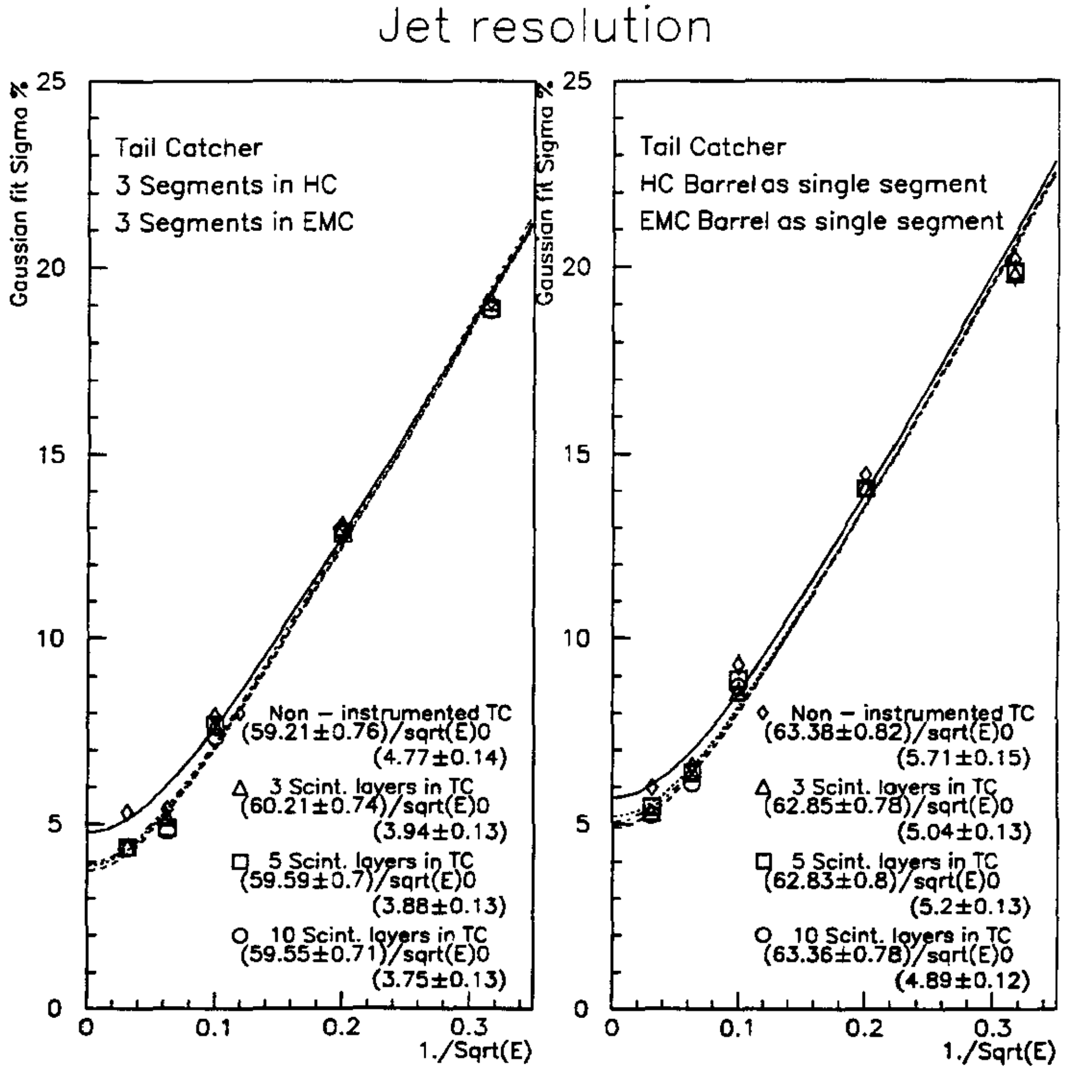

Figure 21: ***Parametrization of jet resolution.***

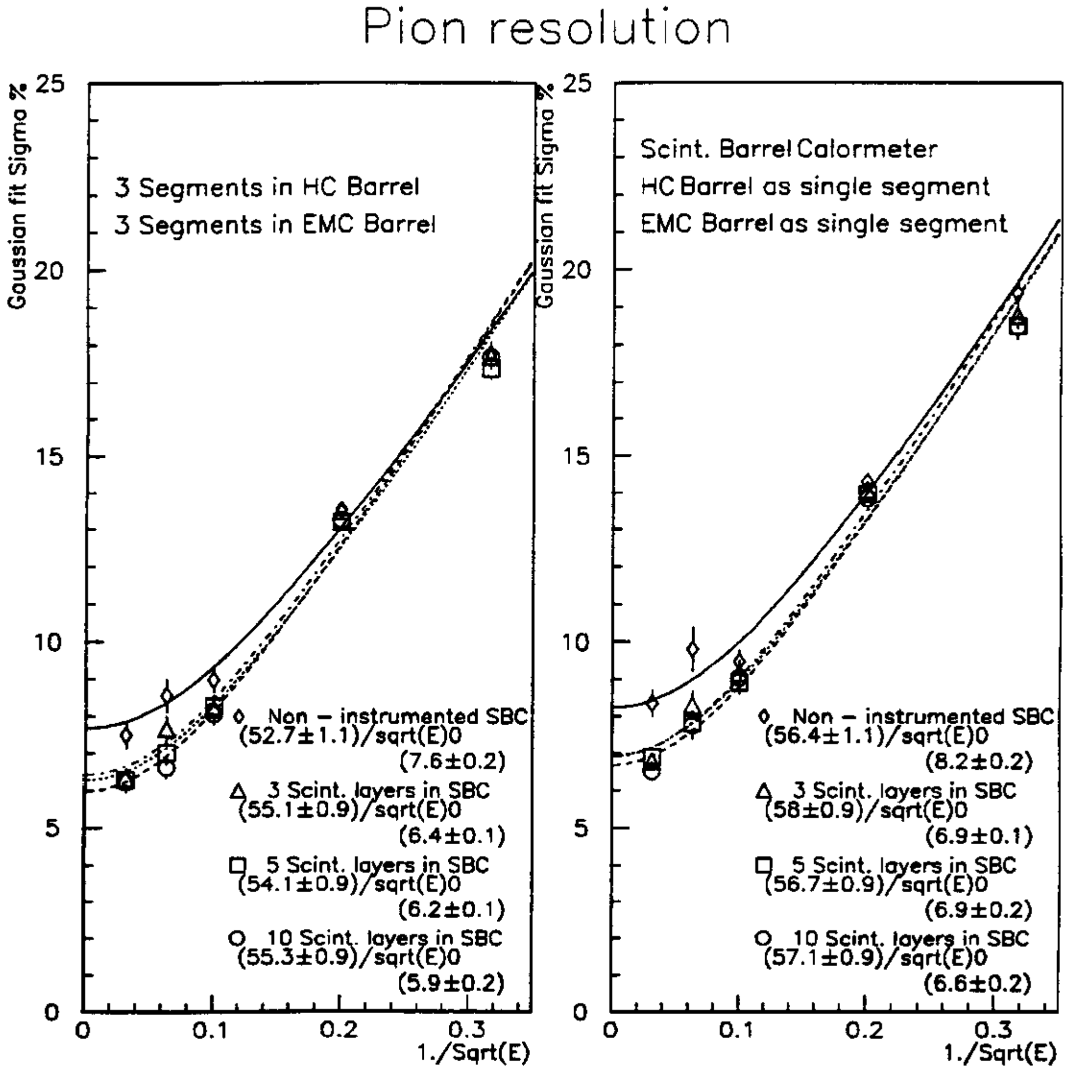

Figure 22: *Parametrization of pion resolution.*

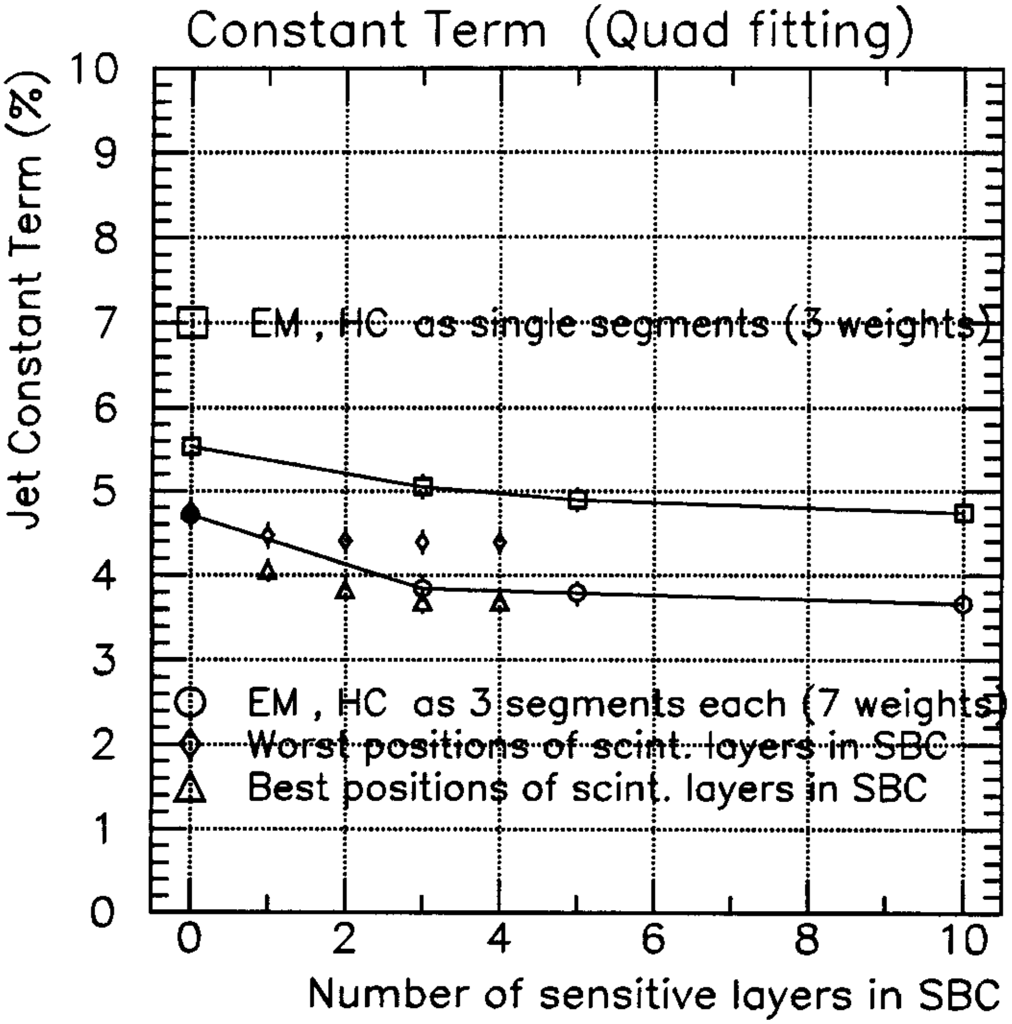

Figure 23: *Constant term for different instrumentation of SBC.*

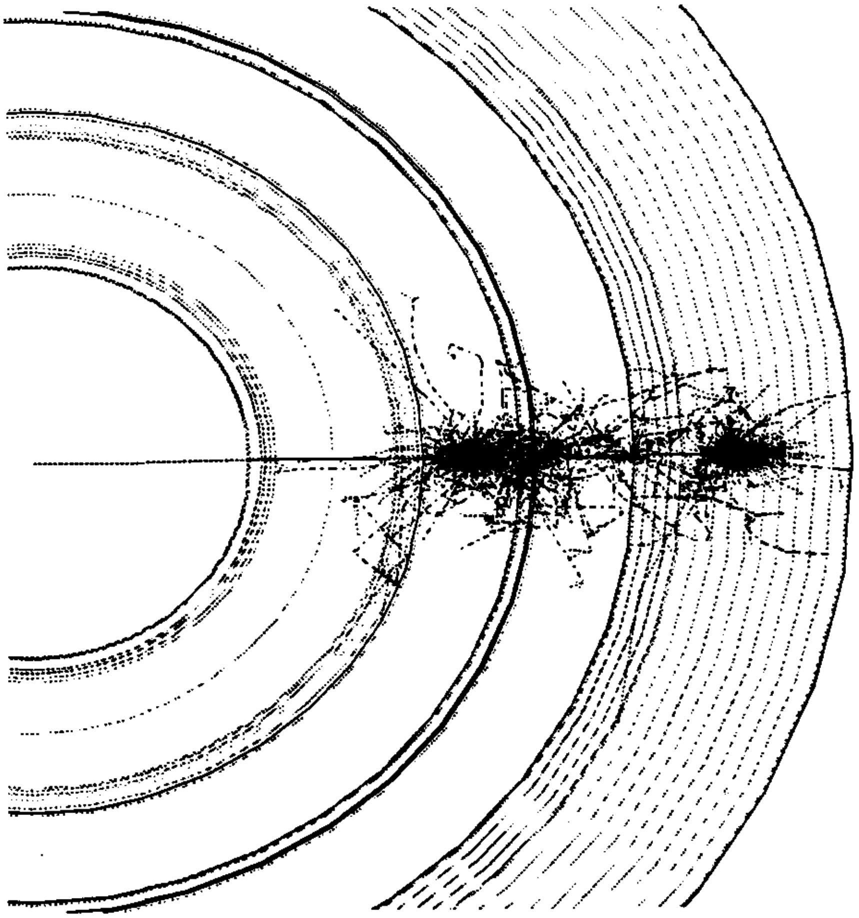

Figure 24: *100 GeV* π^- *shower at* $\eta = 0$. *An example of the hadron event with high energy deposition in the SBC. Two sections of EM Pb/LKr calorimeter, interface to HC modules, two modules of HC, support and cryostat walls and SBC are shown from the inner to the outer radius.*

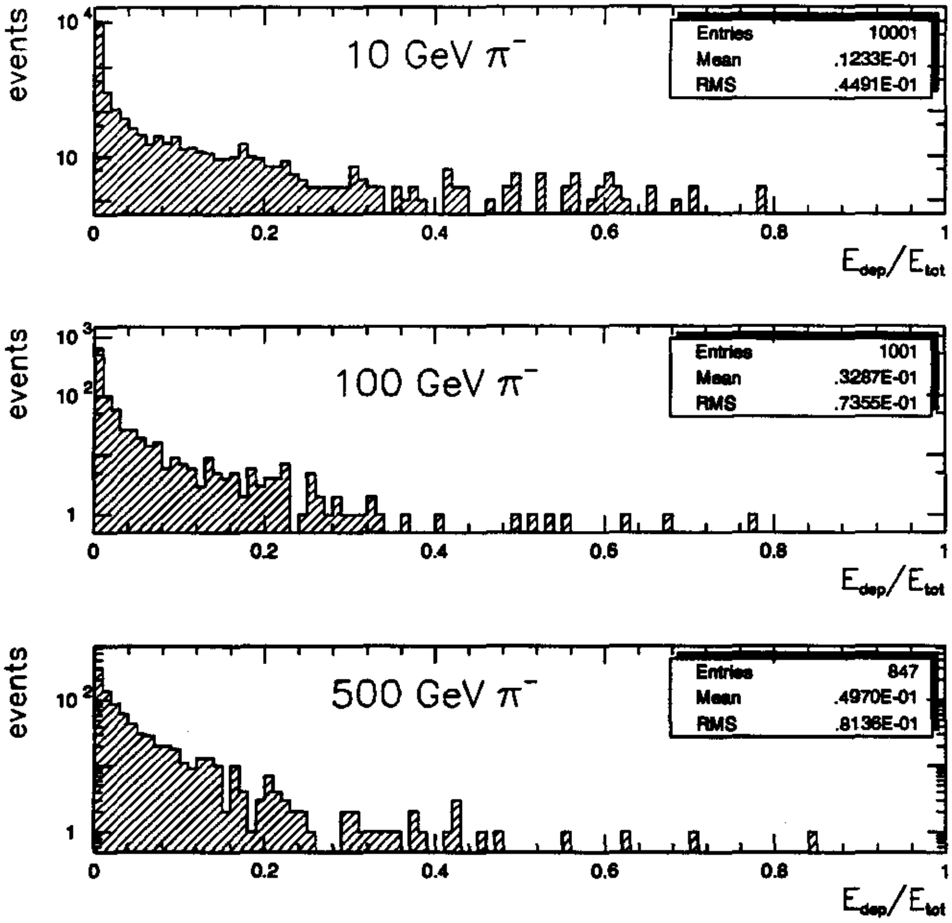

Figure 25: *Spectra of 10, 100 and 500 GeV π^- in the SBC at $\eta = 0$, after 6λ of liquid calorimeters. The average energy deposition in the SBC is 1.2% at 10 GeV, 3.3% at 100 GeV and 5.0% at 500 GeV. One can see events with more than 300 GeV deposition in the SBC at 500 GeV incident energy.*

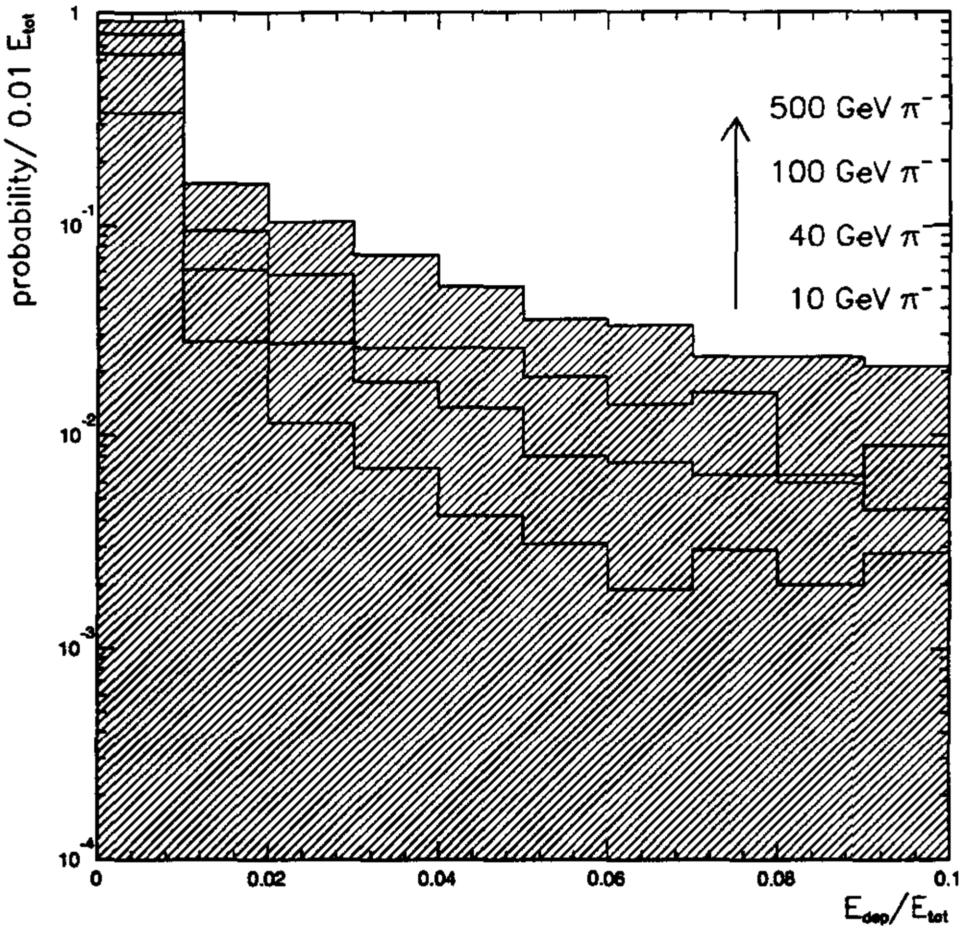

Figure 26: *Parameterization of the hadron energy loss in the SBC at $\eta = 0$, following 6 λ of inner calorimeters. The probability is plotted in bins of 0.01 E_{tot} as a function of the ratio E_{dep}/E_{tot} – fraction of the total energy deposited in the SBC. The scale ranges from 0 to 0.1 E_{tot}. From 10 to 500 GeV the probability ratio increases about a factor of 10 in the tail of the distribution.*

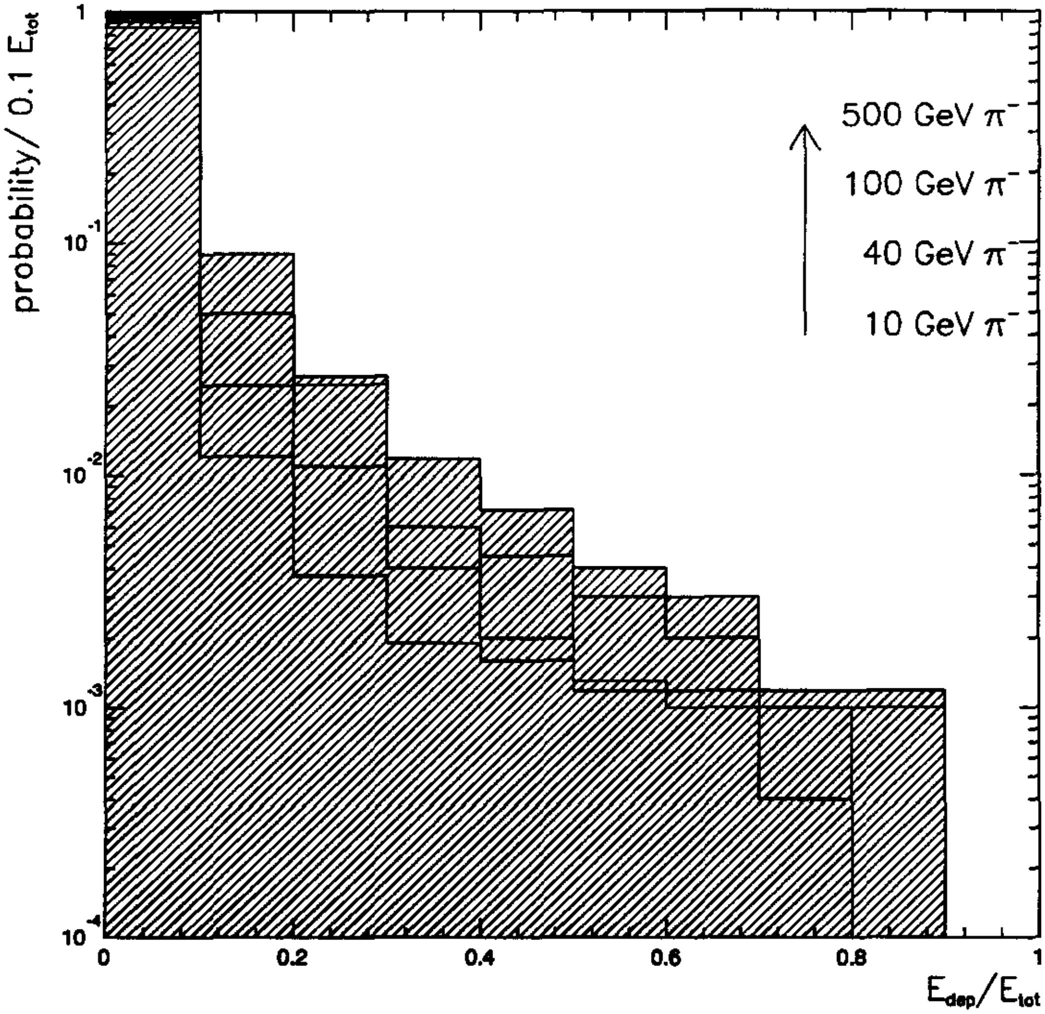

Figure 27: *Parameterization of the hadron energy deposition in the SBC at $\eta = 0$, following 6 λ. The probability is plotted in bins of 0.1 E_{tot} as a function of the ratio E_{dep}/E_{tot}, i.e., the fraction of the total energy deposited in the SBC. The scale ranges from 0 to E_{tot}. One can see that the histograms look similar and differ by a factor of 2-3 in the tails of the distributions.*

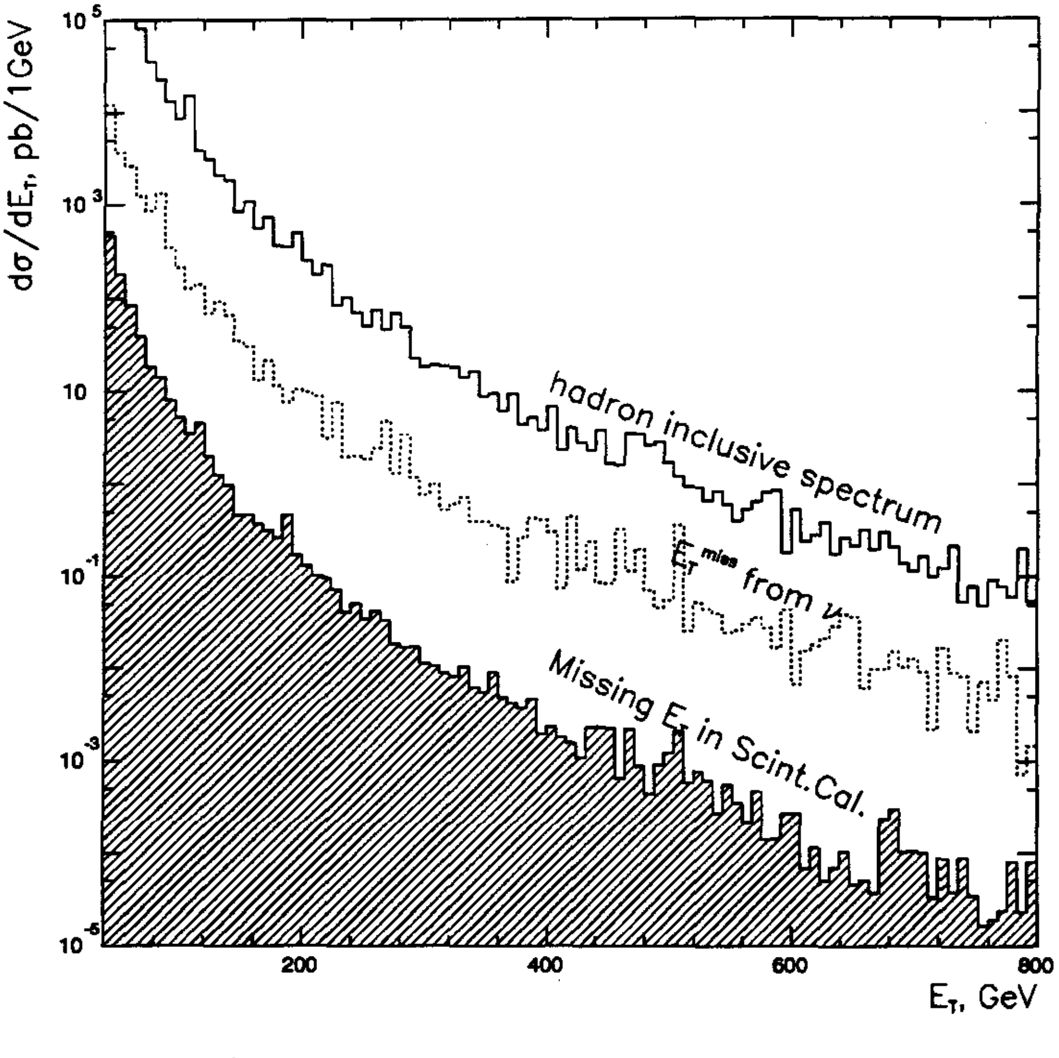

Figure 28: *E_T^{miss} spectrum originated in SBC compared to hadron inclusive cross-section from jets $|\eta| < 1.2$. Also E_T^{miss} Standard Model background is shown (dotted line).*

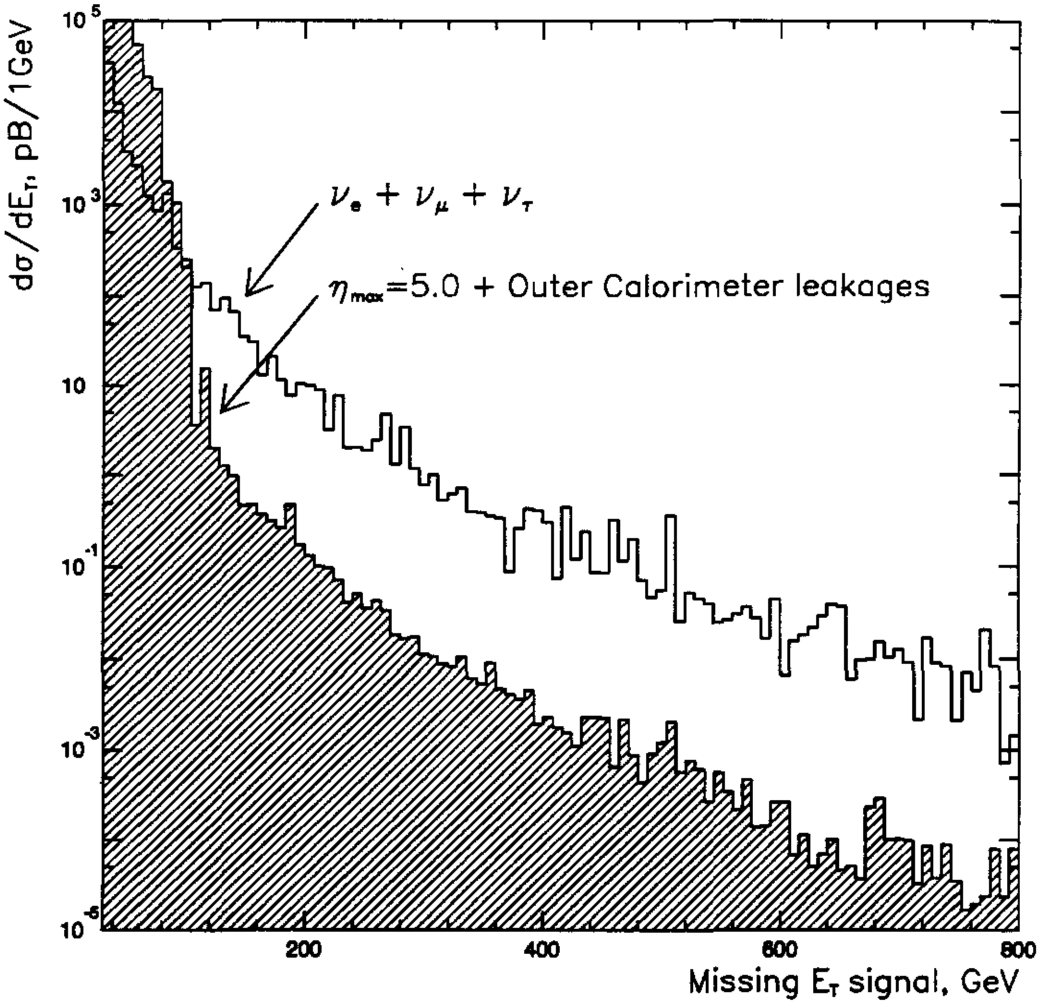

Figure 29: *The effect of limited calorimeter coverage ($|\eta| < 5$) and of E_T^{miss} spectrum in the case of a non-instrumented SBC as a function of E_T^{miss}.*

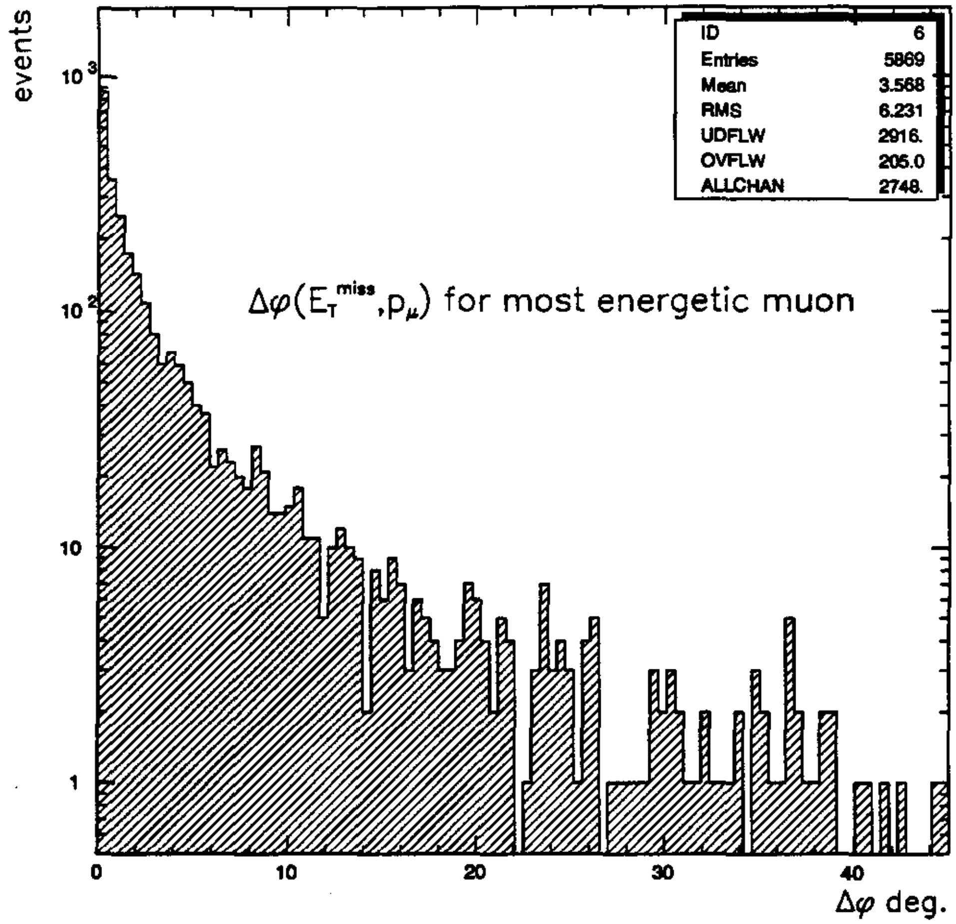

Figure 30: *The angle $\Delta\phi$ between missing E_T vector and the most energetic muon in the event. E_T^{miss} includes leakages into region $|\eta| > 5$. Only events with $E_T^{miss} > 20$ GeV and $p_T^\mu > 20$ GeV in the region $|\eta_\mu| < 2.5$ are included in the analysis.*

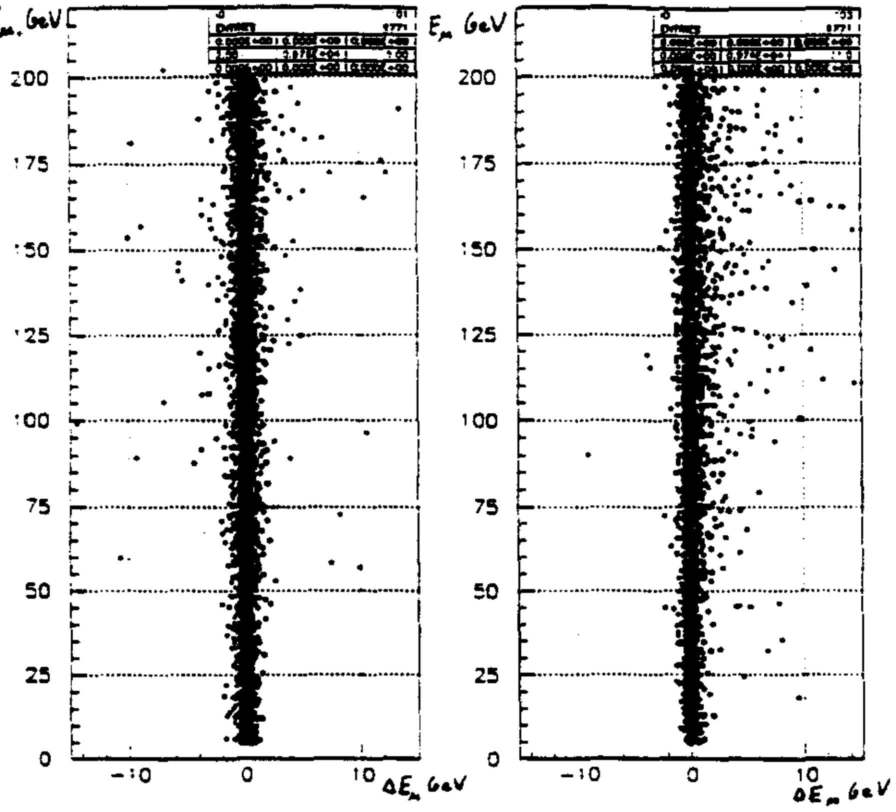

Act

Pass

Figure 31: *Residual muon reconstruction accuracy for instrumented and non-instrumented SBC versions. Perfect resolution of the muon system is assumed.*

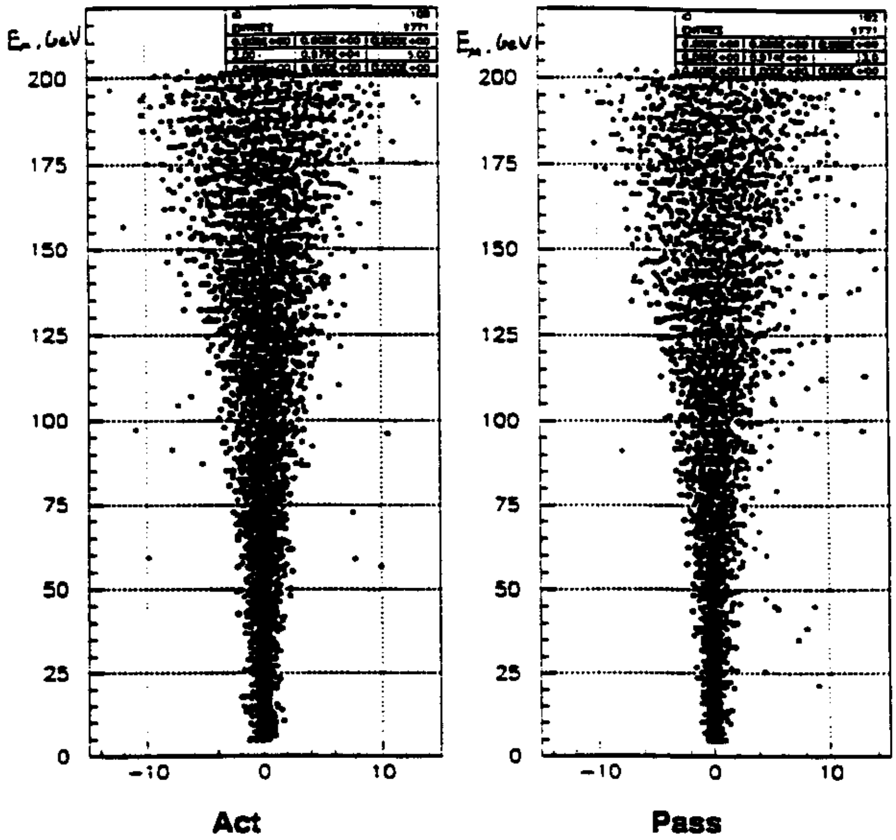

Figure 32: *Residual muon reconstruction accuracy for instrumented and non-instrumented versions of the SBC. Resolution of the muon system as described in Baseline 2 is assumed.*

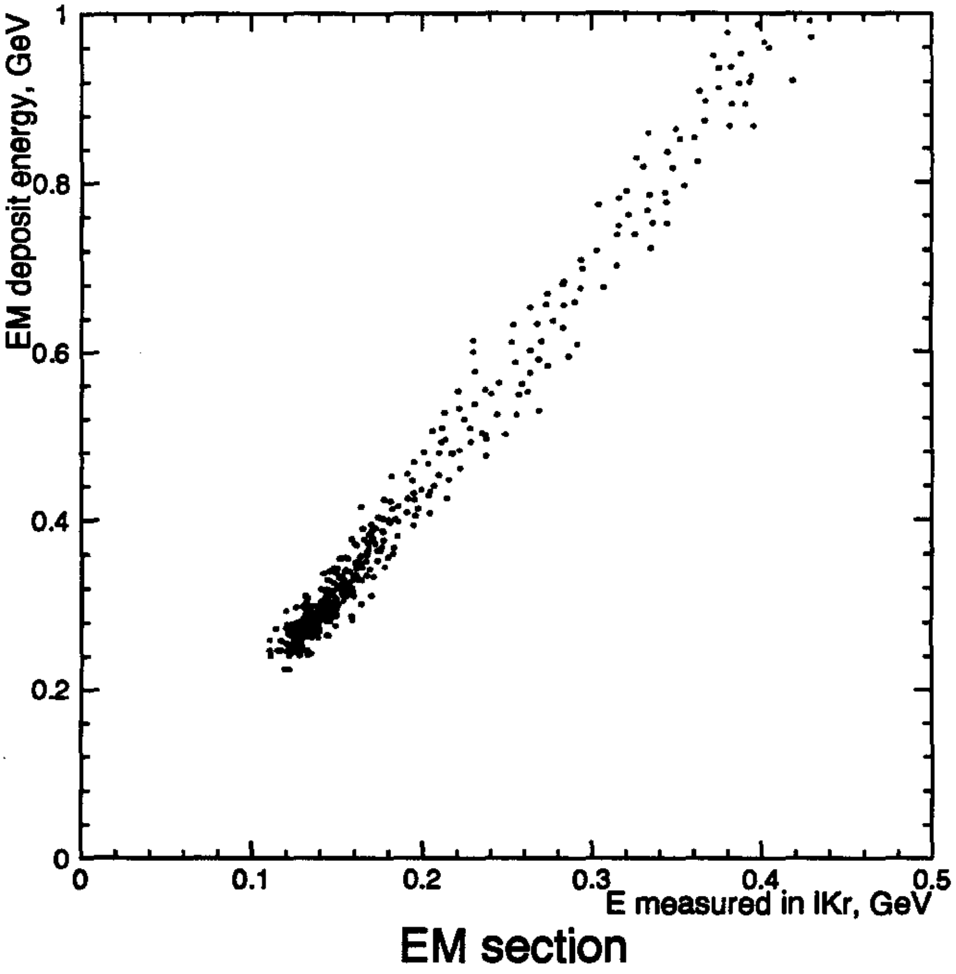

Figure 33: *Muon energy loss vs energy measured in the LKr EM section. The muon energy is 20 GeV.*

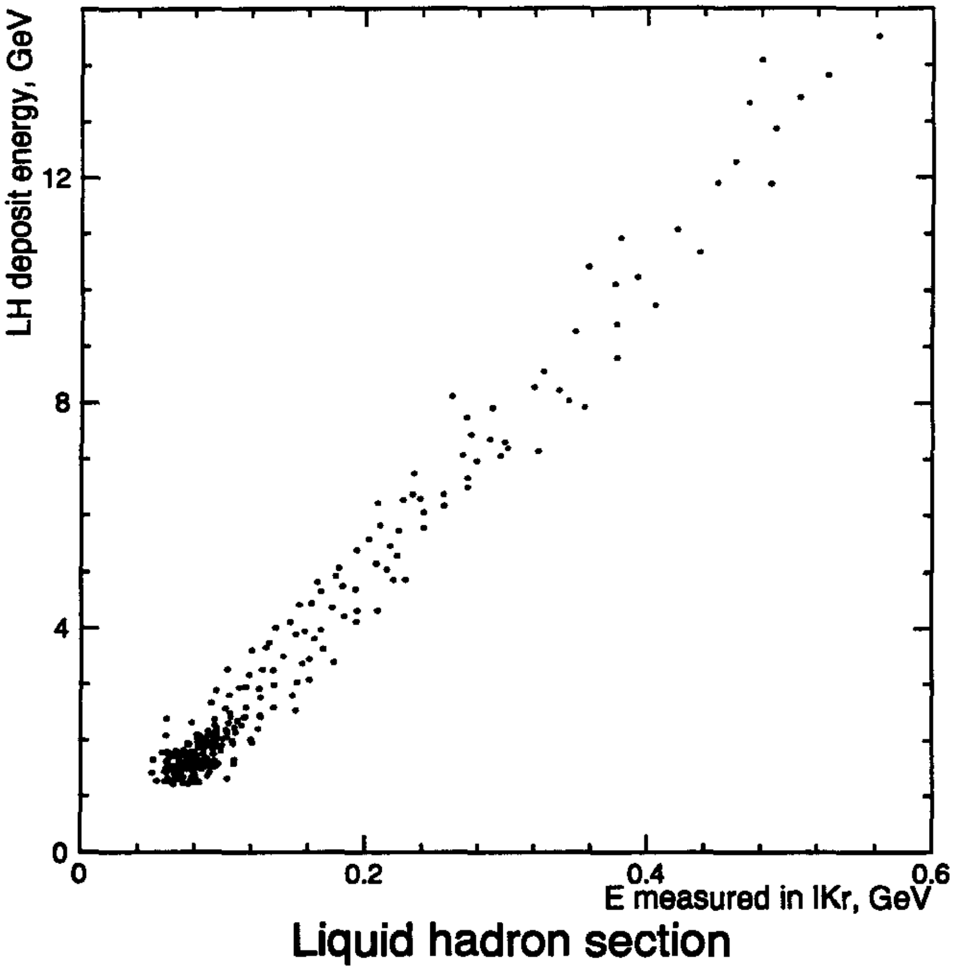

Figure 34: *Muon energy loss vs energy measured in the LKr Hadron section. The muon energy is 20 GeV.*

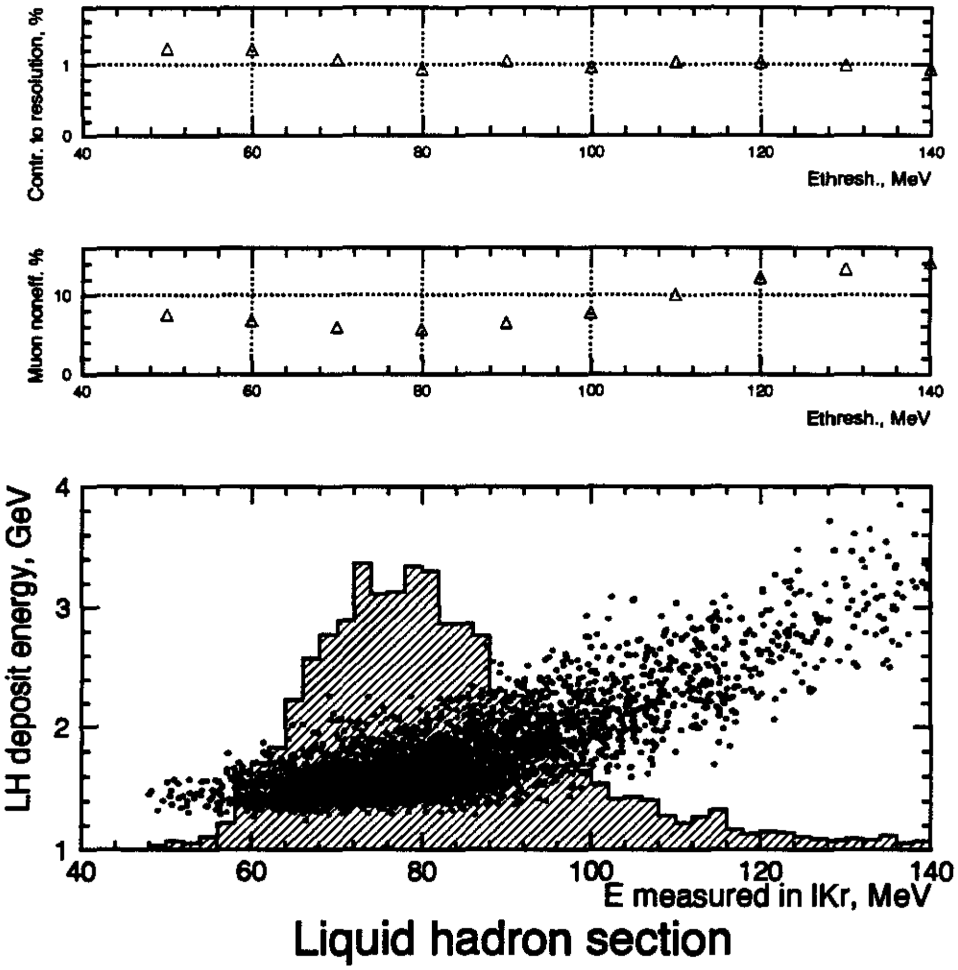

Figure 35: *20 GeV muons near $\eta = 0$. From top to bottom: calorimeter (6λ) contribution to the resolution vs E_{thresh}; muon inefficiency vs E_{thresh}; and muon energy loss vs energy measured in the LKr hadron section. In the lowest portion the projection on the $E_{measured}$ axis also is shown.*

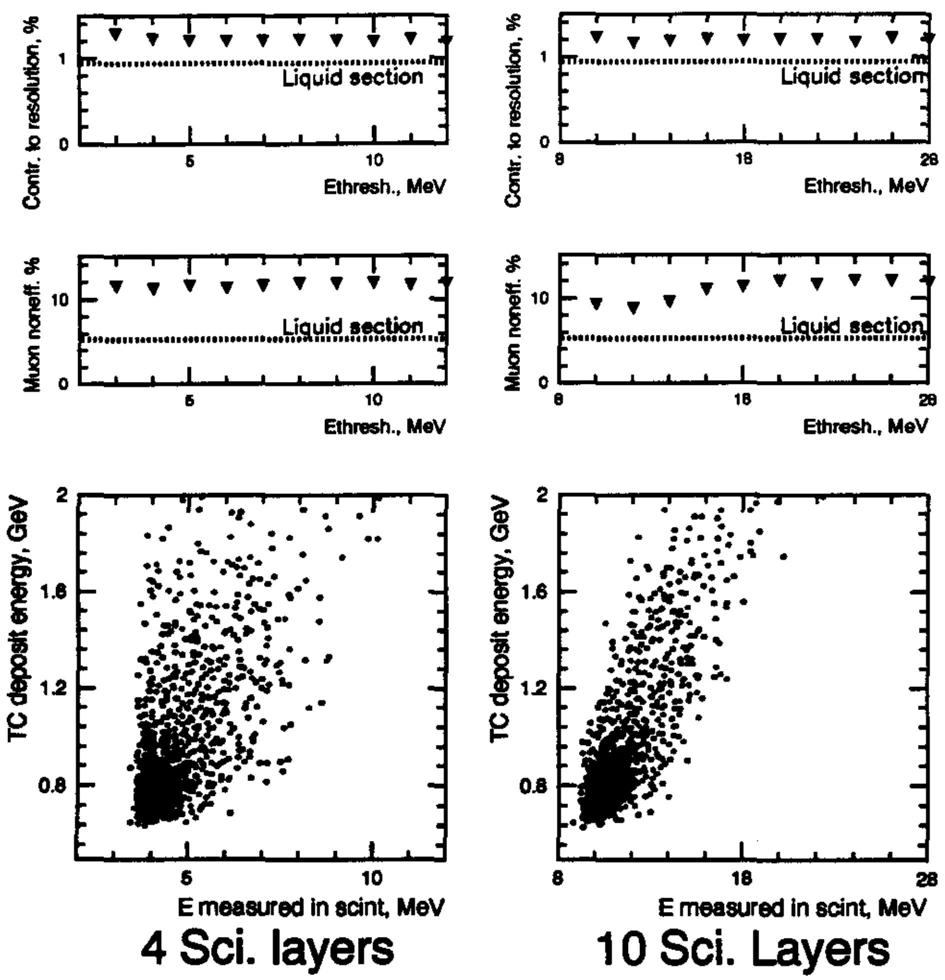

4 Sci. layers

10 Sci. Layers

Figure 36: *20 GeV muons near* $\eta = 0$. *From top to bottom: calorimeter (10.5*λ*) contribution to resolution vs.* E_{thresh}. *Muon inefficiency vs* E_{thresh}. *Muon energy loss vs energy measured in the SBC. The two figures are for 4 and 10 scin. layers in the SBC. The dotted line is the performance of a* 6λ *calorimeter only.*

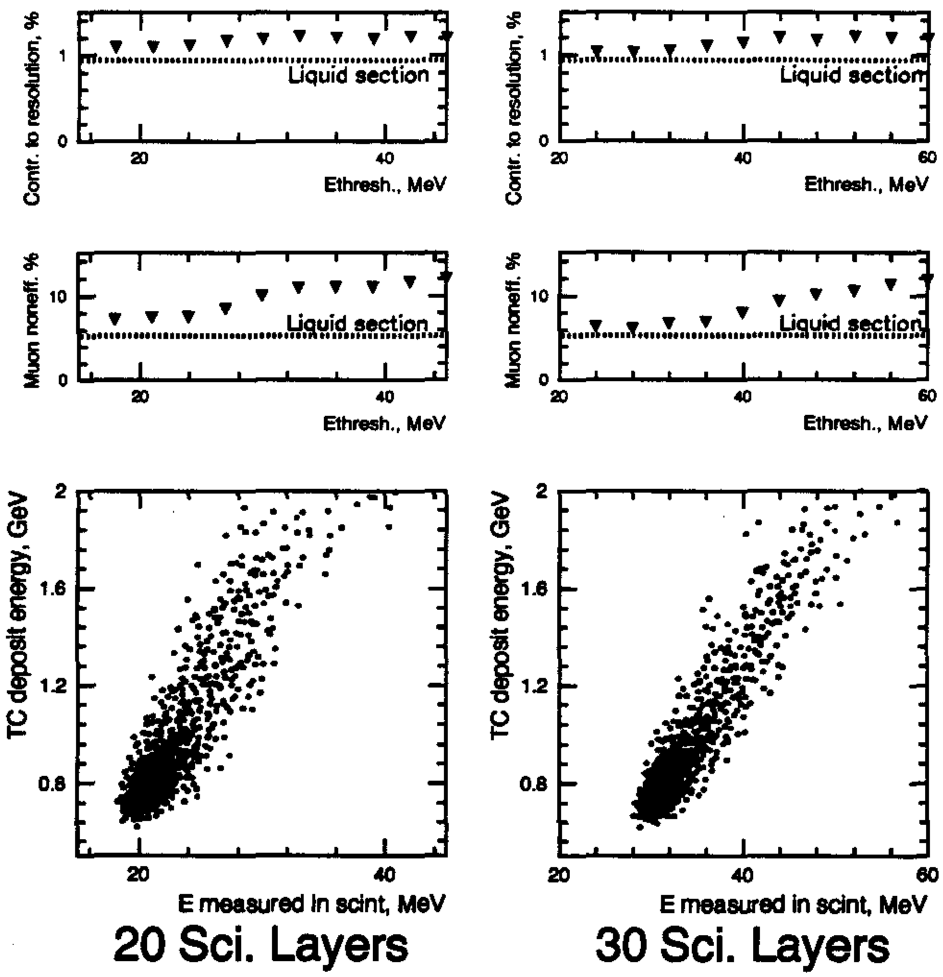

Figure 37: *20 GeV muons near* $\eta = 0$. *From top to bottom: calorimeter (10.5*λ*) contribution to the resolution vs* E_{thresh}. *Muon inefficiency vs* E_{thresh}. *Muon energy loss vs energy measured in the SBC. The two figures are for 10 and 30 scin. layers in the SBC. The dotted line is the performance of a 6*λ *calorimeter only.*

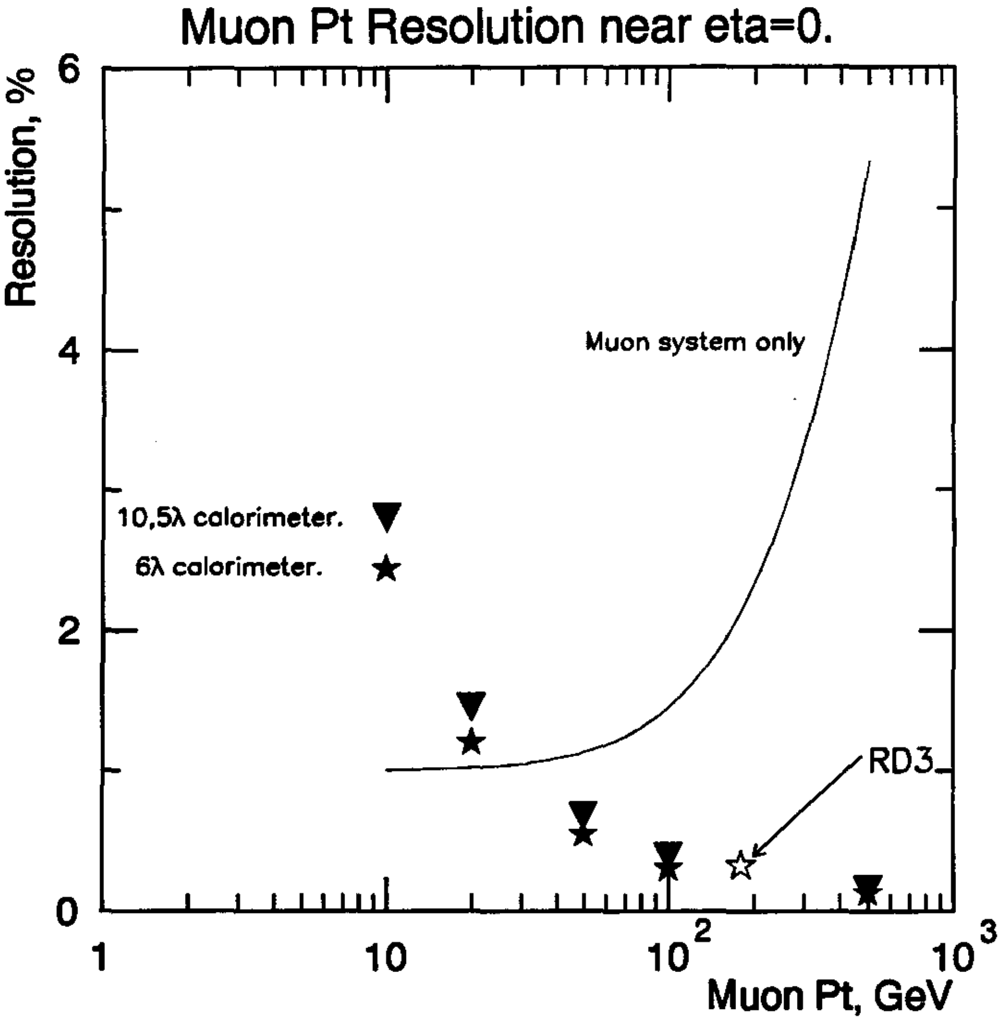

Figure 38: *Contributions to the muon P_t resolution from calorimeter and muon systems near $\eta = 0.$. Stars are for a 6λ calorimeter, triangles for a 10.5λ calorimeter. The open star is the RD3 collaboration measurement for 180 GeV muons. The solid line represents the resolution of the muon system.*

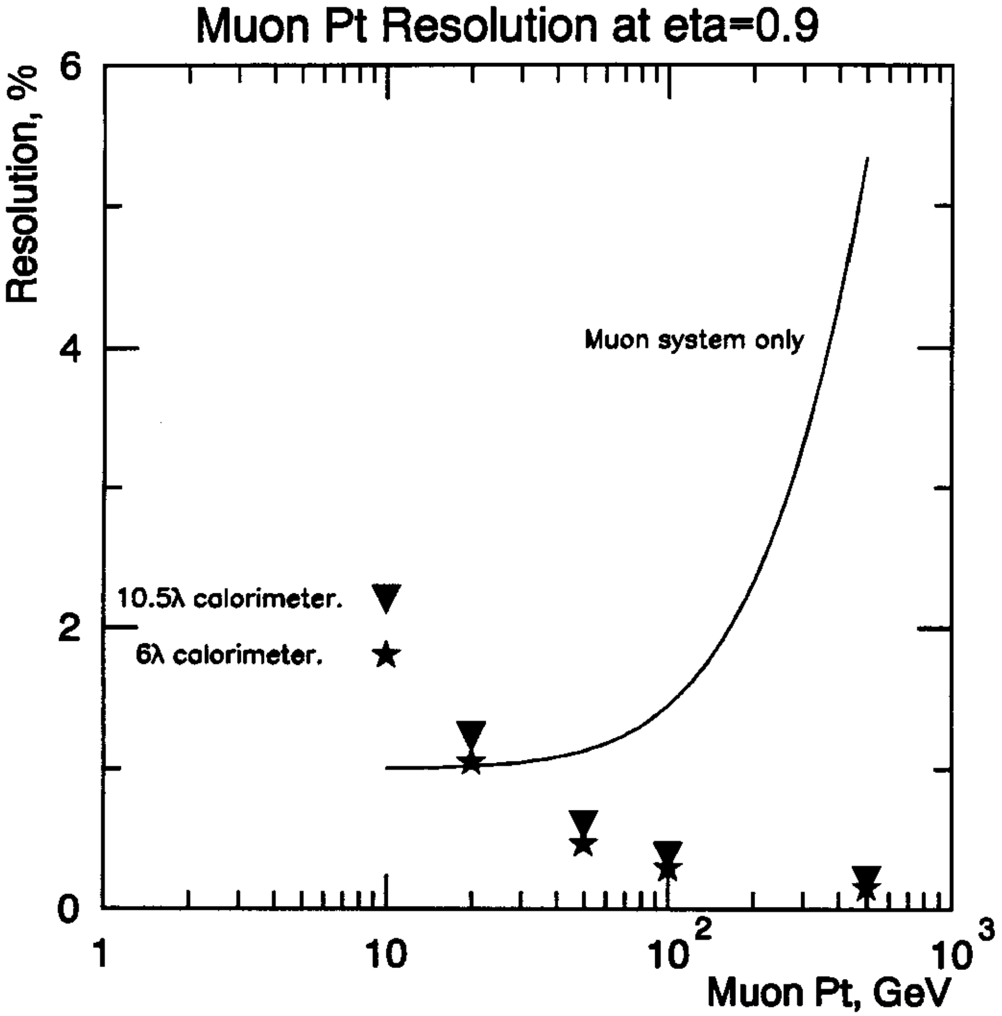

Figure 39: *Contributions to the muon P_t resolution from the calorimeter and the muon system near $\eta = 0.9$. Stars are for a 6λ calorimeter, triangles for a 10.5λ calorimeter. The solid line depicts the resolution of the muon system.*

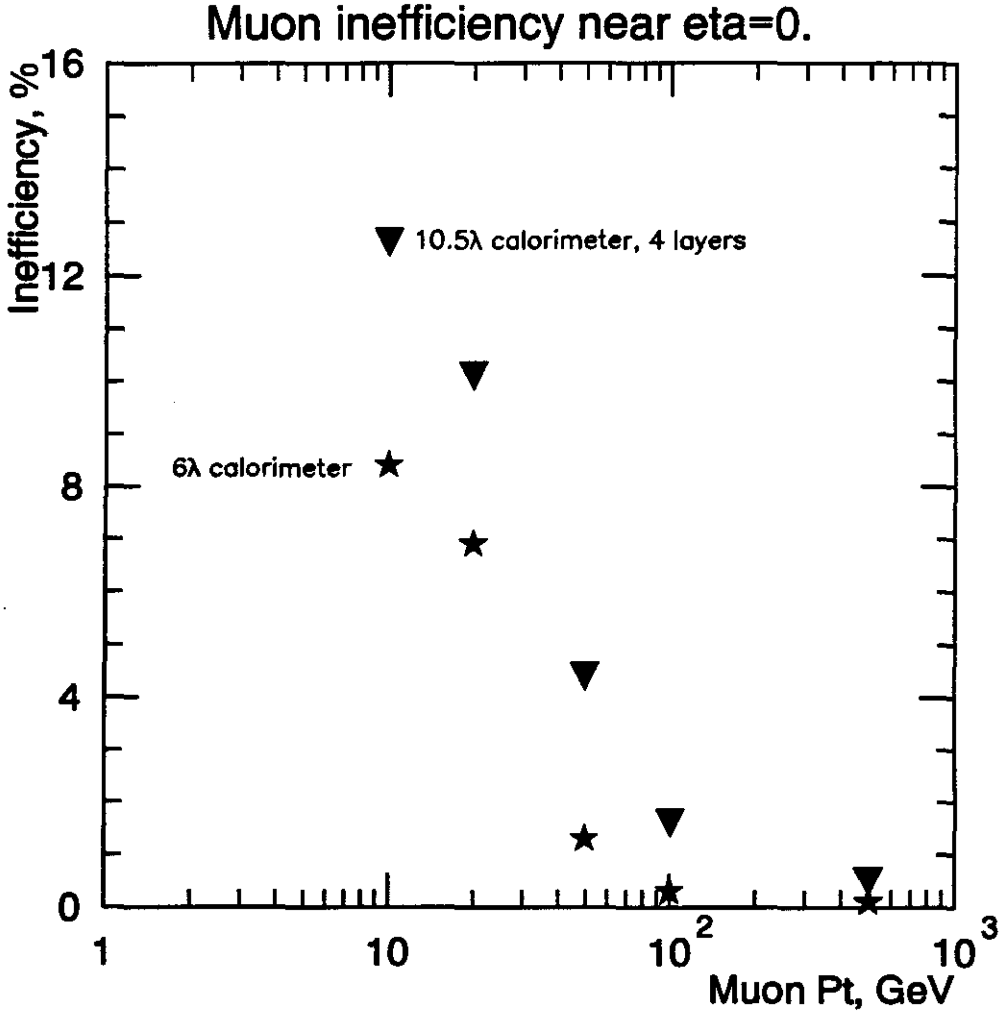

Figure 40: *Muon inefficiency near* $\eta = 0$. *Stars represent a 6λ calorimeter, triangles a 10.5λ calorimeter.*

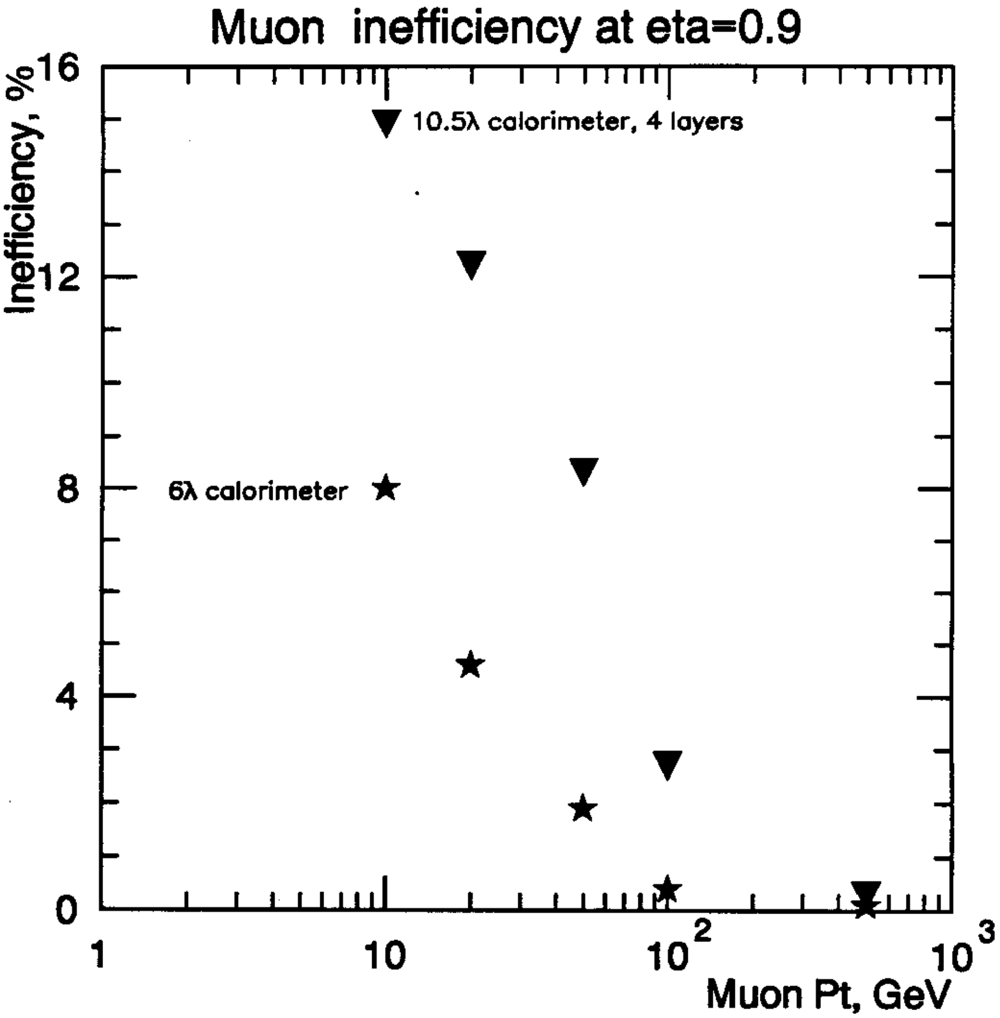

Figure 41: *Muon inefficiency near* $\eta = 0.9$. *Stars represent a 6λ calorimeter, triangles a 10.5λ calorimeter.*

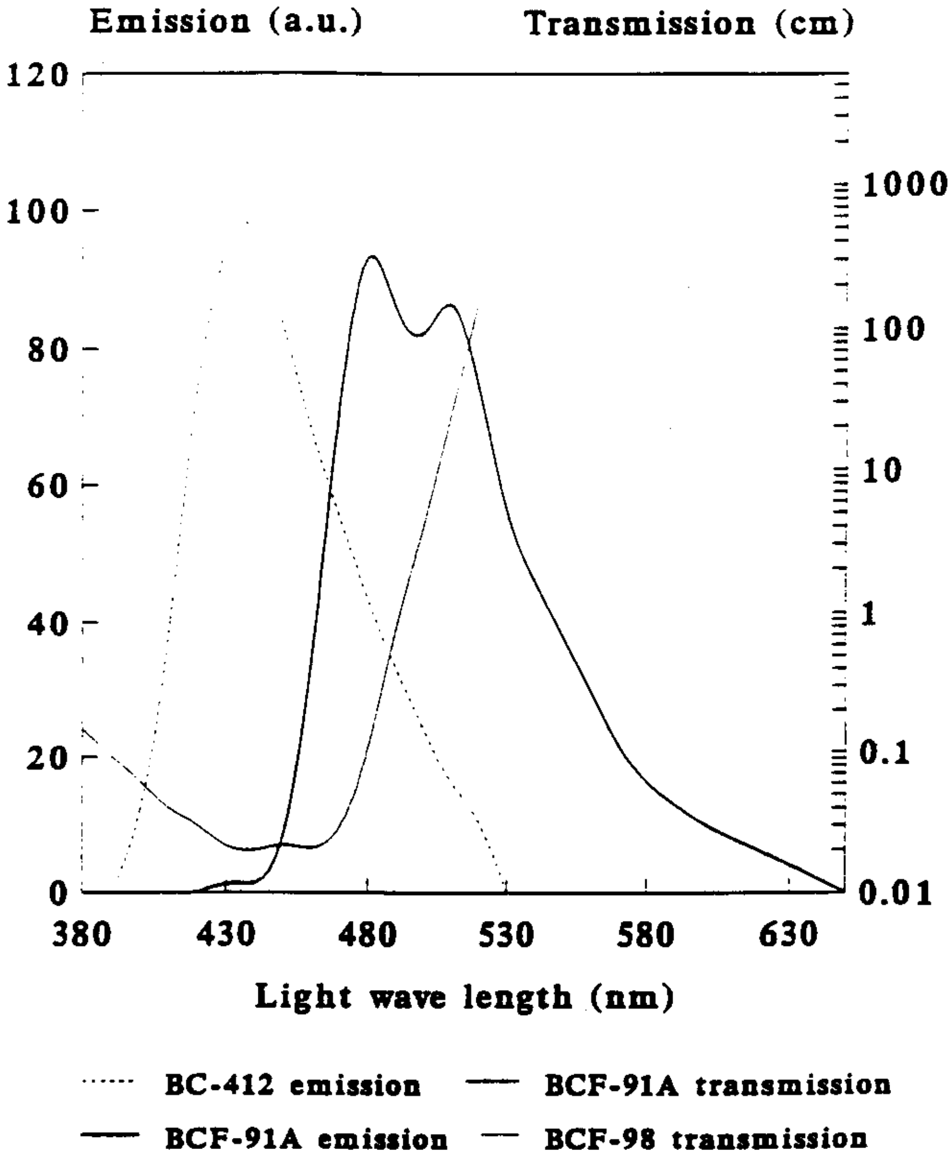

Figure 42: *Spectral properties of materials used in LTRANS.*

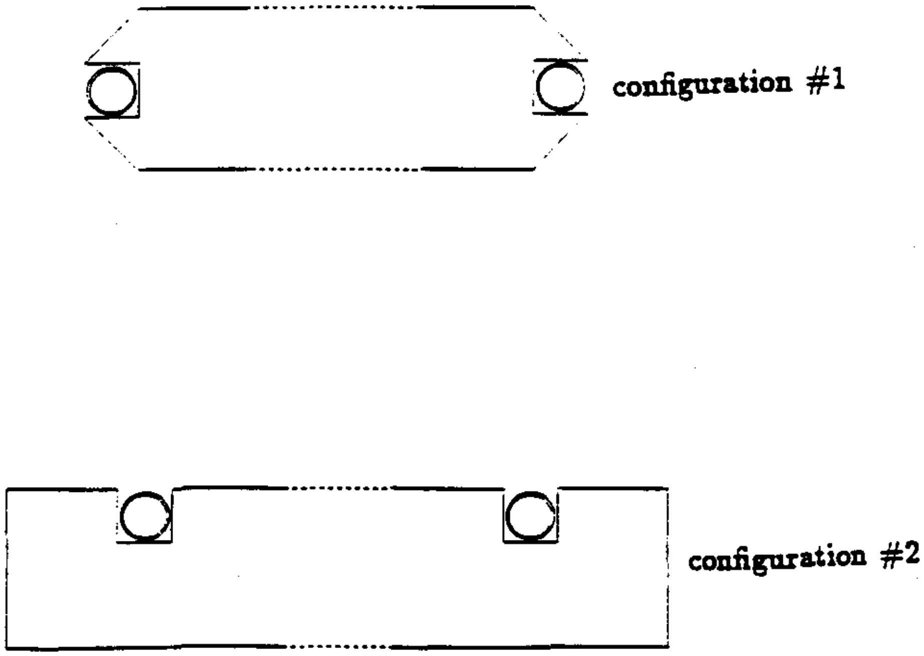

Figure 43: *Two configurations of tile/fiber coupling studied by means of the LTRANS code.*

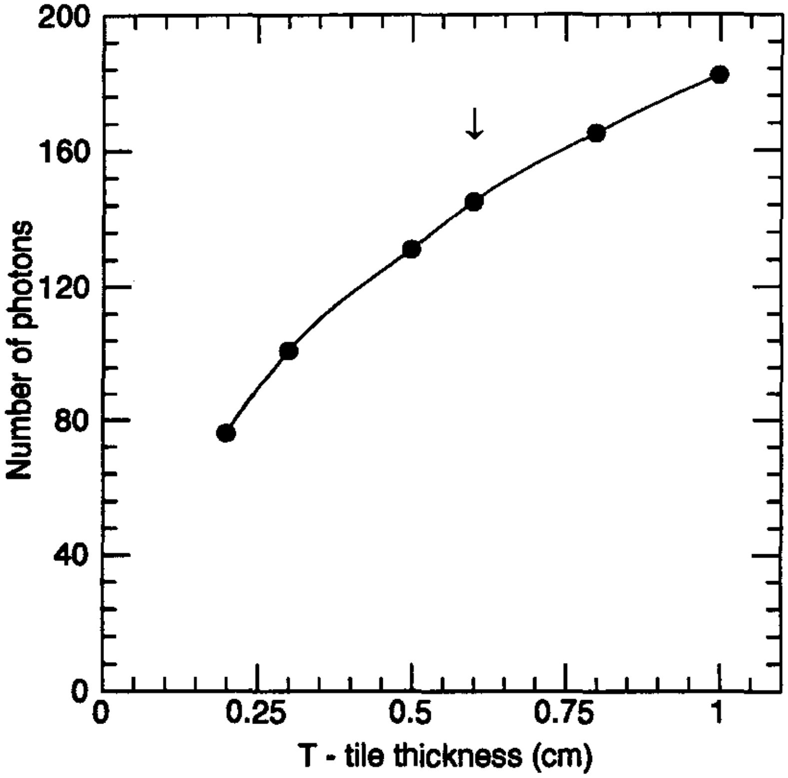

Figure 44: *Number of photons per MIP collected at the photodetector vs tile thickness. Tile area size: 50 * 9 cm^2, 2 WLS fibers of 1-mm diameter glued in grooves; aluminized mylar wrapping; 1-m-long clear fiber.*

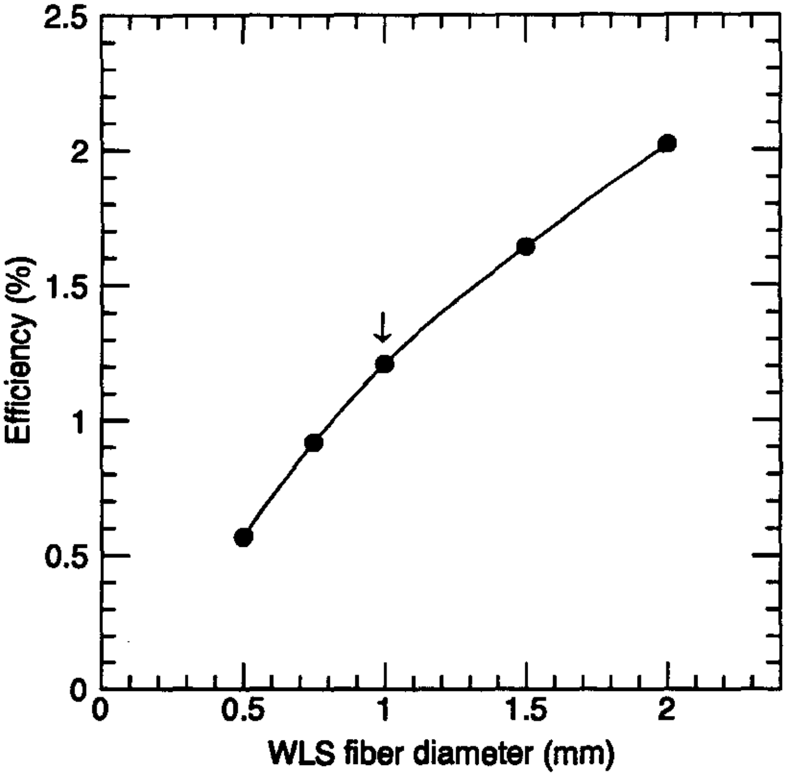

Figure 45: *Light collection efficiency vs fiber diameter. Tile size: 50 * 9 * 0.6 cm*^{3}*; 2 WLS fibers glued in grooves; aluminized mylar wrapping, 1-meter-long clear fiber.*

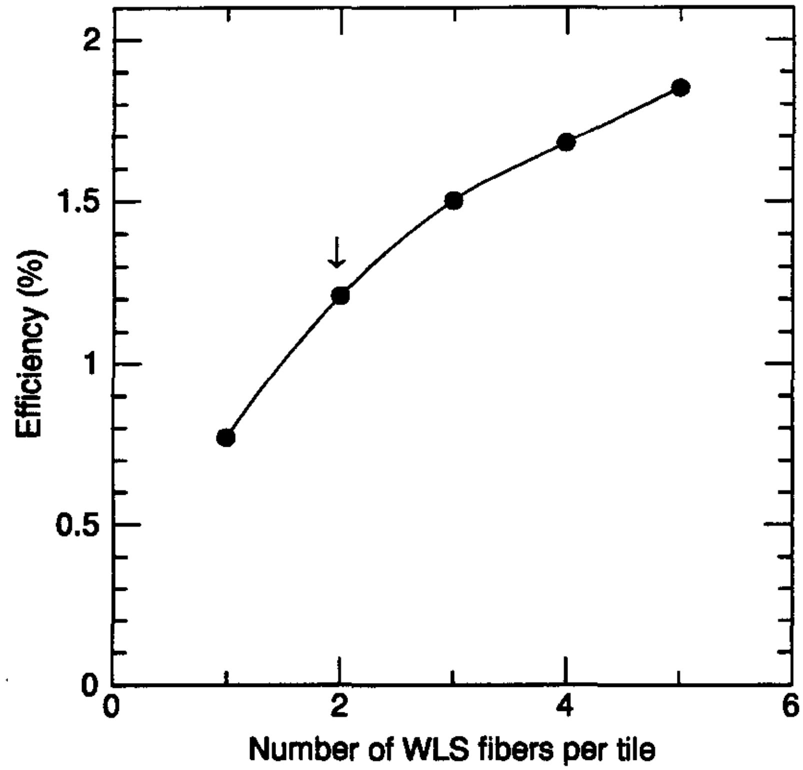

Figure 46: *Light collection efficiency vs number of WLS fibers. Tile size: 50 * 9 * 0.6 cm^3; WLS fibers of 1-mm diameter glued in grooves, aluminized mylar wrapping; 1-meter-long clear fiber.*

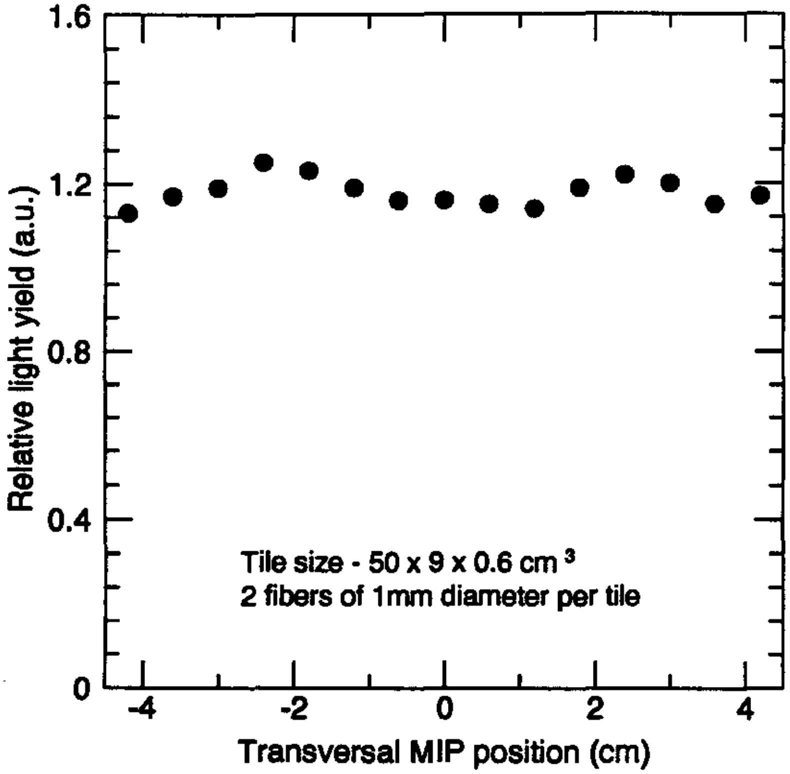

Figure 47: *Transverse nonuniformity of tile response for 2-fiber readout. Tile size: 50 * 9 * 0.6 cm^3; WLS fibers of 1-mm diameter glued in grooves; aluminized mylar wrapping; 1-meter-long clear fiber.*

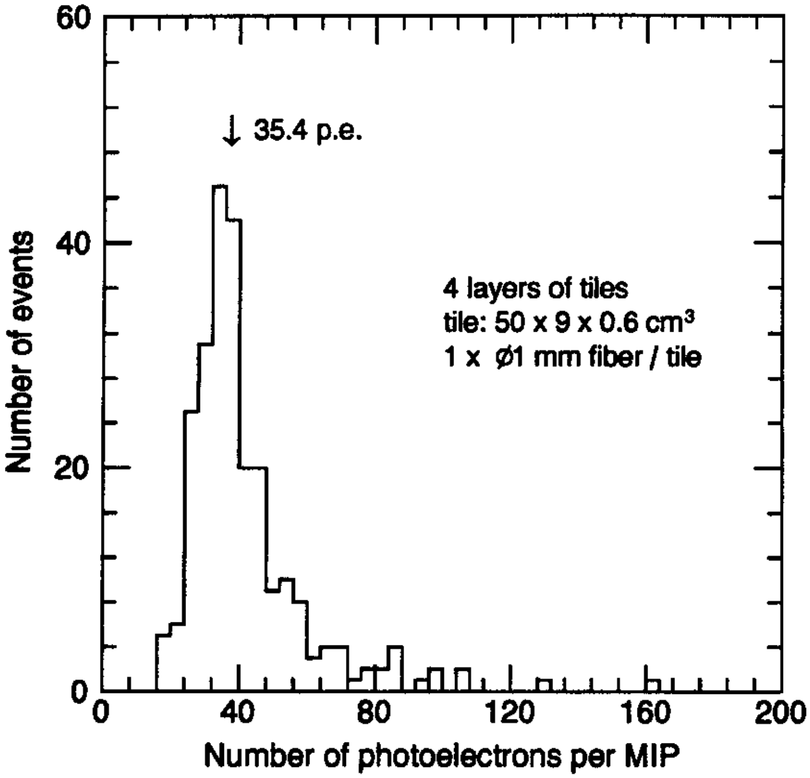

Figure 48: *Response of 4-layer tower to 50 GeV/c muons with 1 glued in WLS fiber of 1-mm diameter.*

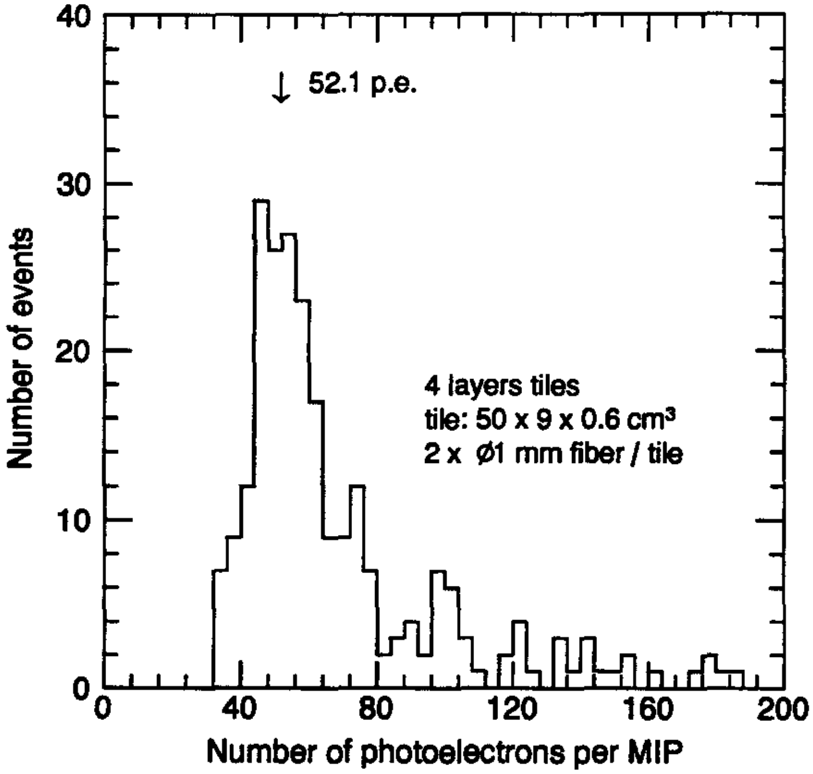

Figure 49: *Response of 4-layer tower to 50 GeV/c muons with 2 glued in WLS fibers of 1-mm diameter.*

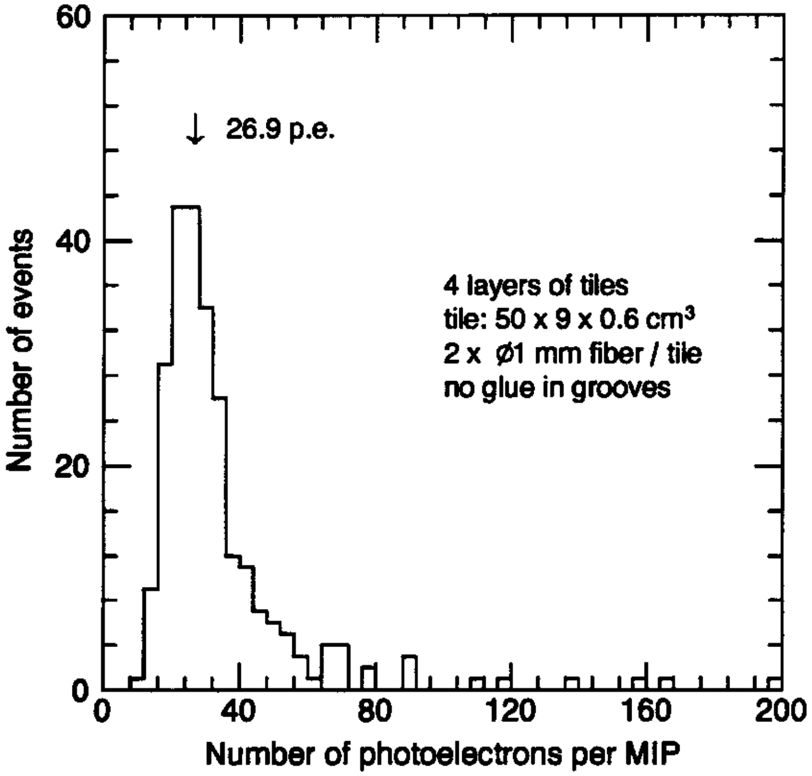

Figure 50: *Response of 4-layer tower to 50 GeV/c muons with 2 not glued in WLS fibers of 1-mm diameter.*

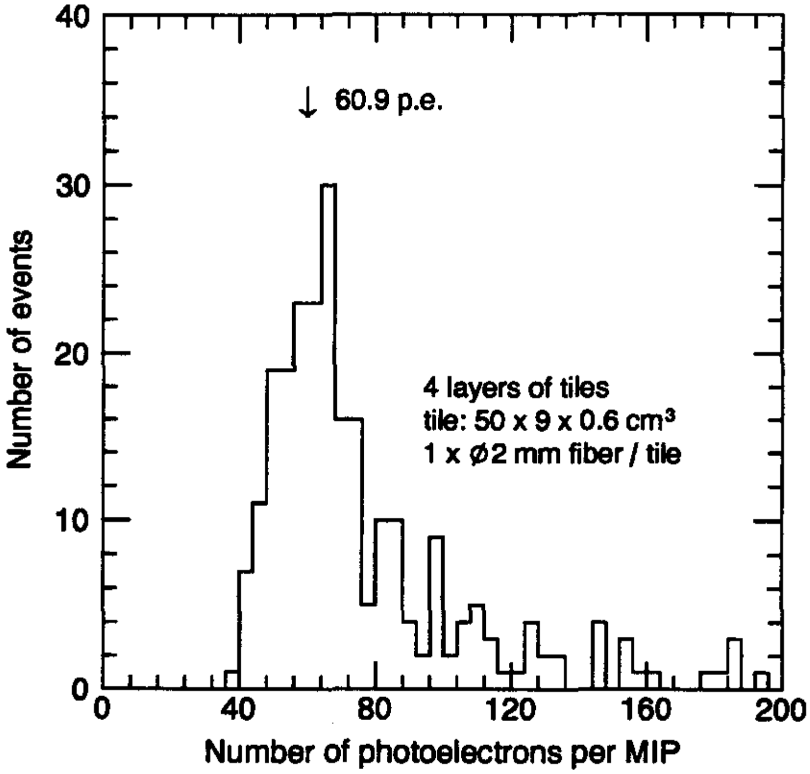

Figure 51: *Response of 4-layer tower to 50 GeV/c muons with 1 WLS fiber of 2-mm diameter glued in.*

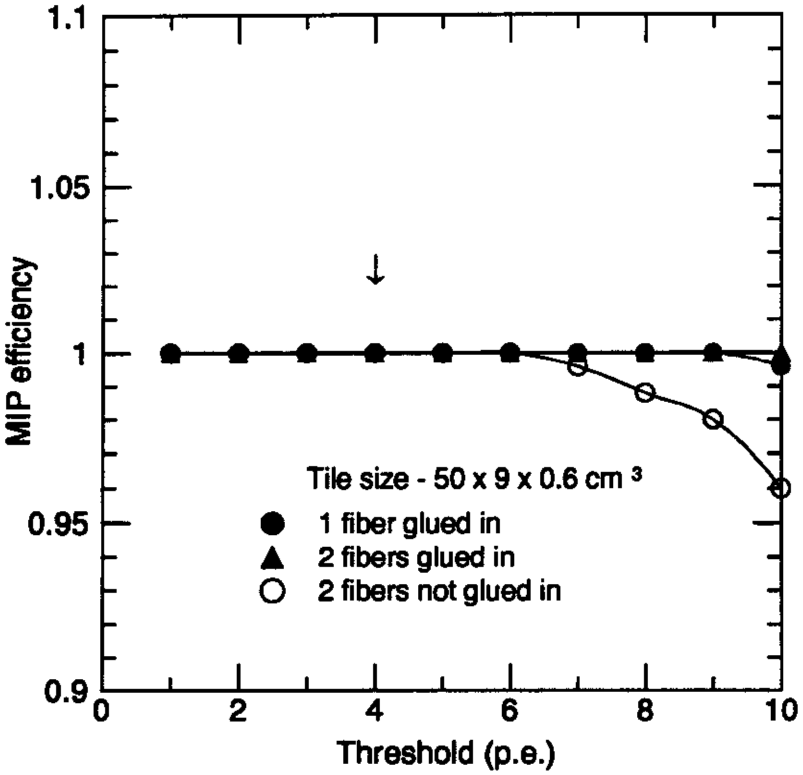

Figure 52: *Efficiency of MIP registration vs threshold for different readout schemes for a 4-layer tower.*